NASA Technical Memorandum 89005

DESIGN AND DEVELOPMENT OF A MULTIBEAM 1.4 GHz PUSHBROOM MICROWAVE RADIOMETER

R. W. LAWRENCE, M. C. BAILEY, R. F. HARRINGTON, C. P. HEARN, J. G. WELLS, W. D. STANLEY

SEPTEMBER 1986

INTRODUCTION

The measurement of multiple geophysical parameters from orbiting spacecraft achieving high spatial resolution, global coverage and frequent revisits is very important and useful in agriculture, hydrology and weather- and climate-forecasting applications. Passive radiometry in the microwave portion of the electromagnetic spectrum would enable all-weather day/night measurements of important geophysical parameters. In particular, geophysical parameters such as soil moisture, sea surface temperature, wind speed, rain rate, snow and ice measurements, and atmospheric parameters can be measured using microwave radiometers.

Microwave radiometers have been used from stationary platforms, aircraft and spacecraft to measure geophysical parameters. Soil moisture measurements of both bare and vegetated fields have been made from trucks (ref. 1), aircraft (ref. 2) and Skylab (ref. 3). Sea surface temperature measurements have been made from aircraft (ref. 4) and spacecraft, including both Seasat (ref. 5) and Nimbus-7 (ref. 6). Salinity measurements have been made from aircraft (refs. 4, 7, and 8). Wind speed and rain rates during severe storms over water have been made from aircraft (ref. 9). Ice measurements have been made from aircraft (ref. 10) and Nimbus-7 (ref. 11). Snow measurements have been made from aircraft (ref. 12) and Nimbus-7 (ref. 13). Atmospheric parameters such as temperature profiles, liquid water content and water vapor have been measured from several spacecraft including Seasat, Nimbus 5, 6, and 7, and SMM/I on DMSP (refs. 14, 15, 16, and 17).

The Antenna and Microwave Research Branch has been developing passive microwave radiometers since 1970. The first precision radiometer developed operated at 2.65 GHz. This radiometer was a balanced Dicke switched analog radiometer employing the noise injection feedback principle. The S-band radiometer was flown on the NASA C-54 during 1972 making precision sea surface temperature measurements (ref. 18). A companion L-band radiometer was built and flown along with the S-band unit on the C-54. Precision measurements of sea surface temperature and salinity over the Chesapeake Bay were made with these instruments (ref. 4). A variable frequency radiometer was developed which operated from 4.5 to 7.2 GHz. This radiometer, the Stepped Frequency Microwave Radiometer (SFMR) (ref. 19) has flown many missions measuring ice parameters, wind speed and rain rate (refs. 20 and 21). Other radiometers developed during the past 14 years include a UHF radiometer operating at 611 MHz, a 34-GHz radiometer and the multiple beam Pushbroom Microwave Radiometer (PBMR).

The simultaneous achievement of high spatial resolution along with wide across track coverage requires the application of either a scanning narrow beam or multiple narrow beams. The multiple beams can either be scanned across track or fixed across track in so-called pushbroom configuration. Since the measurement of soil moisture and sea surface temperature requires low microwave frequencies, the requirement of narrow beamwidths for high spatial resolutions dictates the use of physically large antennas. The use of scanning to obtain the required swath widths becomes a substantial mechanical problem (ref. 22). An airborne prototype of a multiple beam pushbroom microwave radiometer was developed by NASA LaRC to advance the radiometric technology necessary for application to remote sensing of Earth related geophysical parameters.

This prototype would aid in the investigation of possible pushbroom technologies such as Microwave Integrated Circuit radiometer receivers, digital signal processing within the radiometer, local oscillator distribution and other problems associated with the simultaneous operation of multiple radiometric receivers. The Pushbroom Microwave Radiometer (PBMR) prototype was designed to conform to the specifications listed in table 1. These requirements were developed in conjunction with Goddard Space Flight Center personnel involved in the study of the remote sensing of soil moisture. Thus, in addition to a valuable technology research tool, the PBMR will also be a valuable remote sensing tool and will aid in this soil moisture research. The development of the PBMR was initiated in 1979, completed in 1982 and flight tested in 1983. Several operational soil moisture flights were made during 1983 and 1984.

This report describes the actual prototype developmental unit, including brief descriptions of each of the major subsystems and components. Following a brief overview of the noise-injection feedback system and switching process, the discussion proceeds from the antenna and front-end portions through the control and data acquisition system. Block diagrams and major subsystem component specifications are provided where appropriate.

INSTRUMENT DESCRIPTION

Noise Injection Radiometric Technique

A radiometer is a receiver designed to measure the noise power emitted by an object. The level of this received signal is extremely small and is in fact generally smaller than the noise level generated within the receiver. The gain provided by the receiver as well as the receiver noise must be extremely stable since fluctuations in either would result in an error in the radiometer measurement. A Dicke radiometer is one in which the receiver is alternately switched between the desired input signal and a reference noise source (see fig. 1). Following filtering and amplification, a correlation switching operation is performed to down-convert the desired signal from the Dicke frequency to dc. The receiver noise appears as a common mode component. The result is an effective cancellation of the effects of receiver noise on the measurement accuracy.

The noise injection process establishes the Dicke radiometer as a closed-loop feedback system. Noise is added to the input signal such that the mean value of the input signal plus injected noise is equal to the mean value of the reference noise. This process nearly eliminates the effects of gain fluctuations on the measurement.

System Overview

A simplified block diagram providing an overview of PBMR is shown in figure 2. An L-band front-end provides the hardware for noise injection, filtering, input Dicke modulation, and amplification. Control inputs from the digital signal processing unit provide noise injection and the operation of the Dicke switch.

The mixer-amplifier stage is used to down-convert the desired frequency band to a near-zero intermediate frequency (IF). A 1.413-GHz local oscillator is used to perform the down-conversion.

The amplifier/square-law detector stage provides an output voltage proportional to the noise power input. The output of the detector is then processed by a video band-pass filter.

The analog signal processor performs the Dicke correlation of the noise signal. This switching operation is controlled by the digital signal processor. The output is smoothed by a low-pass filter.

The digital signal processor provides the appropriate algorithm for optimum loop filtering and data estimation.

Each of the individual sections will now be discussed in detail.

Antenna and Feed Network

The antenna is a 64-element (8 by 8) array of V-dipoles with a stripline feed network for producing multiple beams. The V-dipole was selected as the array element because its radiation pattern is nearly circularly symmetric about the beam axis and also because its projected length is shorter at resonance than a linear dipole, thus allowing closer physical spacing of the elements (0.45 wavelengths for the present array). Each row of eight dipoles is fed with a corporate feed network designed so as to excite the row of elements with a tapered amplitude distribution which approximates a cosine function, thus providing a low sidelobe (-23 dB) radiation pattern along track. The eight rows are then combined through a modified Butler matrix network to produce simultaneous beams at discrete angular scan positions across track. The Butler matrix has been modified so as to provide the flexibility of selecting either 4 beams with a uniform amplitude excitation or 3 beams with a cosine amplitude excitation by replacing a single printed circuit board. Both configurations provide a high degree of isolation between beam feed ports and utilize the full array aperture for each beam. The primary performance difference between the two configurations is the sidelobe level (-13 dB versus -23 dB) in the cross-track direction.

A photograph of the dipole array is shown in figure 3, and the back of the array is shown in figure 4, in which the stripline feed network is visible. The dipole elements are oriented with respect to the feed network so as to provide beam scan in the H-plane of the array. The feed network is modularized and the composite network is assembled by interconnecting SMA coax to stripline transitions. This modularization allows individual portions of the network to be acceptance tested prior to assembly. Selection of the 3-beam or the 4-beam option is accomplished by replacing the topmost printed circuit board.

The stripline circuit layout for one of the rows of eight elements for producing a cosine amplitude excitation along track is shown in figure 5. The amplitude taper is achieved through the use of unequal but inphase power-dividers. The design of these power-dividers is described in (ref. 23).

A schematic of the 8-element Butler matrix network, which has been modified for three beams with a cosine amplitude distribution, is illustrated in figure 6. The circuit is madeup of two-way equal power-dividers, quadrature hybrids, and fixed phase-shifters. The schematic for the four-beam uniform amplitude network is illustrated in figure 7. The horizontal dashed line in figures 6 and 7 represents the location of the interconnection for the two printed-circuit boards for the physical implementation of the circuit. By separating the circuit at this location, one

3

portion of the circuit will be common to both the 3-beam and 4-beam networks. The networks were fabricated in 1/8 inch stripline with teflon-fiberglass substrate.

The antenna reflection coefficient and isolation between input beam ports was measured with a network analyzer over the frequency range of 1313 MHz to 1513 MHz. The reflection coefficient for the 3-beam configuration is shown in figure 8 for each beam port. Since the reflection coefficient of the center beam, S_{22}, was higher than that of the other two beams, an inline matching transformer was designed to be used on the center-beam input port so as to present a better impedance match near the center frequency. The dashed curve in figure 8 shows the reflection of the center-beam port with the matching transformer installed. The isolation between input ports for the 3-beam configuration is shown in figure 9. The isolation was measured as the power transmission between pairs of input ports with the unused port terminated in a 50 ohm load. The reflection coefficient for the 4-beam configuration is shown in figure 10 and the isolation between input ports is shown in figure 11.

The far-field radiation pattern for each beam of the array was measured in an anechoic chamber with all other beam input ports terminated in 50 ohm loads. These pattern data are presented in the appendix.

Radiometer Front-End

The L-band front-end consists of commercial coaxial subassemblies which perform the functions of noise-injection, band-pass filtering, amplification and Dicke switching. These components are mounted on a massive aluminum base plate to facilitate temperature stabilization (see fig. 12). System operation will be explained in a logical sequence following the block diagram of figure 2.

The noise source is a Microwave Semiconductor Corp. Model MC-65198, a dc biased avalanche diode which furnishes an excess noise level ratio of 30 dB. Flatness, or uniformity of output, over the 1,413 ± 50 MHz band is better than 0.1 dB.

The noise modulator is an Anghel Laboratories Model S-013 SPDT PIN diode switch, utilizing a single series diode in each leg. It exhibits an "ON" insertion loss of less than 0.5 dB and an "OFF" isolation in excess of 30 dB. One output port of the switch is terminated so that the noise source is always loaded by 50Ω. The other output port feeds the noise-injection directional coupler through a level-set pad which has a nominal attenuation of 10 dB to produce a ENR of 0 dB at the output of the directional coupler.

The directional coupler is a MAC Technology Model C-3203-20, and it "sums" the input signal with the internally generated noise pulses during the input half-Dicke cycle. Insertion loss in the signal path is typically 0.15 dB, directivity is greater than 27 dB, and the coupling factor is nominally 20 dB.

The input band-pass filter is a K & L Microwave Model 3B340-1413/172 ultra low-loss coaxial type filter. It provides a significant amount of protection from out-of-band interference while exhibiting an in-band loss of typically 0.3 dB. The -3 dB bandwidth is 172 MHz, which results in a -1 dB bandwidth of 100 MHz, which is the full frequency allocation of the radioastronomy band centered at 1.413 GHz.

The Dicke switch is also an Anghel Laboratories Model S-013. It is mounted on top of an aluminum block which envelopes the reference termination and serves as a

4

heat "reservoir" to maintain the termination at a highly stable temperature to facilitate accurate measurements.

Low noise amplification is accomplished with a Tronteck Model L 1413A three-stage bipolar transistor amplifier which provides, nominally, 30 dB gain, a noise figure of 2.4 dB (or noise temperature of 215K), an input return loss exceeding 10 dB, output return loss exceeding 20 dB, and gain flatness over the 100-MHz band of better than 0.4 dB.

The output band-pass filter provides additional selectivity at a point in the system where somewhat higher insertion loss can be tolerated. It is a KW Engineering Model 1413-136.6-5PL miniature 5-pole band-pass filter with a -3 dB bandwidth of 136.6 MHz, a -1-dB bandwidth exceeding 100 MHz and in band insertion loss of 1.2 dB.

The final subsystem associated with the L-band front-end is the Bias Current/ Line Receiver, and it performs the dual functions of providing a highly stable bias current of 5 mA at a nominal level of 28 V dc to the noise source, and it converts the balanced (to ground) control signals for the two PIN diode switches to the required TTL levels. The current regulator uses an AD581 precision voltage reference configured as a constant current source as shown in figure 13(b). The line receivers are DM 7820A's wired as per figure 13(a).

Mixer/Local Oscillator

The Mixer/Amplifier module accepts the 1.413-GHz output signal from the L-band front-end and frequency translates it to an intermediate frequency band centered at zero. (The non-dc response of subsequent video amplifiers effectively produces a "notch" centered at dc with a -3 dB bandwidth of about 1 MHz.) This assembly consists of a flat-pack, double-balanced mixer (Anzac Model MD-614) driving two cascaded modular amplifiers: Watkins-Johnson Models UTO-511 and UTO-502. The overall conversion gain is, nominally, 23.5 dB. At the rated local oscillator drive level of +7 dBm, the input-port VSWR is 1.22 (return loss = 20 dB), which is quite good for a mixer. The band-pass of the entire assembly extends to greater than 400 MHz. Construction is microstrip housed in a machined aluminum enclosure.

The local oscillator is an Anghel Laboratories Model 05-13. It is a fundamental frequency, bipolar transistor oscillator in which frequency is controlled by a microstrip transmission line. This circuit exhibits an excellent frequency-temperature coefficient of only 36 PPM/C, and it provides an output power at 1,413 MHz of +16 dBm.

IF and Video Analog Electronics

The Mixer-Amplifier module is followed by the IF Filter module which, in turn, feeds the Amplifier/Square-Law Detector Module.

The IF is a 7-pole Chebyshev low-pass configuration built on microstrip and housed in an aluminum box. The -3 dB bandwidth was set by operational requirements to be 12.5 MHz, corresponding to a 25 MHz RF bandwidth; however, any bandwidth up to 50 MHz (low-pass) would be compatible with the L-band front-end parameters. Figure 14 contains a schematic diagram, parts data, and measured electrical characteristics of this system element.

The Amplifier/Square-Law Detector consists of two modular amplifiers (Watkins-Johnson Model UT00502 and UT00515) driving a back-diode, square-law detector with post-amplification. This module is schematically depicted in figure 15. The RF transformer provides dc isolation between the "front" and "back" ends of the radiometer to eliminate ground-loops and impedance transformation to match the back diode. The detected signal is amplified by a gain of 30, low-pass filtered at 10 kHz and the output is balanced with respect to ground for transfer to the analog processor via a shielded twisted pair transmission line. The entire IF subassembly including mixer, 12.5 MHz filter, and amplifier/square-law detector is shown in figure 16.

Signal Procesing

The Signal Processing/Temperature Monitoring and Control Subsystem performs radiometer signal processing, temperature monitoring and control and all communication with the Display and Data Acquistion System (DDAS). The Analog Signal Processor hardware consists of four printed circuit boards within the radiometer enclosure. The Digital Processor includes a commercial Intel 88/40 microprocessor board and a custom Counter/Timer board employing 8253 Timers. The signal processing section performs the required radiometer processing on the output of the detector and controls the noise injection pulses to null the radiometer. In addition, the signal processor controls the Dicke switching and performs further averaging of the radiometer loop output before sending it to the DDAS. The temperature monitoring and control section monitors the output of up to 16 thermistors and 4 nickel resistance thermometers, and it can provide up to 12 channels of temperature control. The communication section provides communication with DDAS over a serial bus and handles command characters from the DDAS. A functional block diagram illustrating these three sections is shown in figure 17. In the interest of clarity, each section is represented and will be discussed as if it were totally independent. However, all three sections do share hardware, and in fact, one microprocessor performs all three functions.

Radiometer signal processing.- The differential output of the detector is converted to a single-ended signal by a difference amplifier on the analog processor board. The dc portion of this signal is then removed by a five-pole Butterworth high-pass filter with a cutoff frequency of 10 Hz. This high-pass filter is used to reduce the effect of the inherent 1/f noise within the analog processing electronics. The output of this filter is then demodulated by the same square-wave (with no dc component) which was used to modulate the signal within the radiometer front-end. Thus, as discussed in the description of the Dicke radiometer, the average level of the output from the demodulator is proportional to the difference between the effective reference temperature and the antenna plus injected or feedback effective temperature. This error signal is then used to control the feedback noise power to null the loop. The error signal is filtered by a three-pole Butterworth low-pass filter with a cutoff frequency of 300 Hz. This permits the signal to be sampled at a slower rate; yet it still allows the loop response to be determined by the digital signal processing.

The output of the three-pole, low-pass filter is sampled by a 12-bit analog-to-digital converter (ADC) on the Intel 88/40 board within the Digital Processor, which also provides the Dicke switch drive such that the sampling frequency is four times the Dicke frequency, i.e., four samples per Dicke period. Synchronization of the sampling and Dicke drive provide a substantial reduction of the Dicke ripple of

6

sampled valves (ref. 23). The 12-bit words from the ADC are then processed by the loop algorithm.

The desired closed loop radiometer response is a first order loop with 40 ms rise time. The required transfer function of the signal processor is then an integrator which is implemented digitally as an accumulator, with the discrete transfer function

$$R(z) = \frac{1 + z^{-1}}{1 - z^{-1}}$$

The output of this accumulator then controls the feedback noise pulses. This output is also sent to the post loop processing section.

The noise injection pulses are generated by Intel 8253 programmable timers within the Digital Processor. These timers are programmed as variable one-shots. In this mode, the output of the timer goes low and will remain low for N clock cycles, where N is the digital word loaded into the timer. The timers are triggered by the master clock 32 times per Dicke cycle, and the timer output is used to gate on the noise diode. This generates 16 pulses of variable width during the antenna portion of the Dicke cycle. Thus, the duty cycle of the injected noise pulses and, therefore, the effective feedback temperature is controlled by the digital word loaded into the timer from the accumulator algorithm. This completes the radiometer loop, nulling the error voltage, and providing the desired first-order overall loop response.

Temperature monitoring and control.- The temperature monitoring and control section is an extremely flexible system consisting of four Nickel Resistance Thermometer (NRT) channels providing measurements with sensitivity of 0.05°C which are used to measure the radiometer reference terminations. In addition, there are 16 thermistor channels with sensitivity of 0.1°C, and two channels to measure environmental temperature of the digital signal processor and power supply enclosures (sensitivity 1.0°C). The system includes 12 independent channels of heater control (200 watts each available). The control algorithms are then implemented in software allowing the use of any input sensor or combination of sensors to provide thermal control of an area within the radiometer.

The present configuration consists of four precision Nickel Resistance Thermometers, one on each of the four radiometer front-ends used to monitor and control the temperature of the reference termination, and seven YSI 43201 thermistors located on the instrument deck, three of which are used to control the deck temperature, the others are to be used to evaluate the performance of the thermal system. Three additional thermistors located on the antenna deck are used for control and monitoring of the physical antenna temperature. Finally, two AD590 thermistors are used to measure the power supply and DSP enclosure temperature.

The resistance and thus the temperature of the four NRT's are measured via a constant current source and high-impedance difference amplifier located on each of the four analog boards. The biasing networks for the YSI thermistors are located on Analog Processing boards 1 and 2 (8 each board). The output of the eight thermistors on each board are then multiplexed under control of the microprocessor. On the Intel 88/40 board, the 12-bit ADC samples the four NRT outputs from the difference amplifiers, the thermistor output of the two multiplexers, and the digital signal

processor and power supply enclosure temperatures from the AD590's. This temperature information is then sent to the communication processing portion to be recorded. Selected sensor data are also used in the applicable temperature control algorithm. The outputs of these control algorithms are loaded into 8253 programmable timers, which are used as variable one-shots as discussed in the radiometer processing section above. The outputs of these timers are optically coupled to RCA T2023 TRIAC's which control the heater power, thus controlling the physical temperature.

Post Loop Processing

The post loop processing and communication portion of the signal processor receives the output data from the radiometer and temperature control algorithms, performs further averaging and sends the data to the DDAS.

Radiometer data from each of the radiometer algorithms is sampled by the post loop processor at one-twelfth the loop sampling frequency. (i.e., every twelfth loop sample is taken by the post loop processor). This reduction in sample frequency decreases the correlation between samples, therefore improving the efficency of the post loop averaging. Sixteen of these samples are averaged for each radiometer producing an integration time of 0.5 seconds. This data along with the reference and system temperatures are stored until the completion of the sixteenth post loop sample (every 0.5 seconds) at which point they are transmitted to the Display and Data Acquisition System at 9600 Baud over a standard RS232 bus.

Display and Data Acquisition

The Display and Data Acquisition System (DDAS) is a multi-instrument data handling and recording system utilizing a serial RS232C link to the Pushbroom Microwave Radiometer (PBMR) instrument. It was designed around the requirements of the PBMR but could be incorporated in other aircraft experiments. Figure 18 shows a simplified block diagram of the DDAS. The serial data link to the DDAS has a maximum average data rate of 2 kbits/s. The Pushbroom Microwave Radiometer average data rate is 300 bits/s. The DDAS formats and records the radiometric data with aircraft attitude and position, time code, infrared radiometer (PRT-5) and other ancillary data. DDAS system provides the PBMR instrument operator a real-time display of all recorded data in engineering units and computed brightness temperature in a fixed format. Additionally, the DDAS provides four channel strip chart recorder outputs for in-flight correlation of observed physical ground features (water, sand, etc.) and radiometric brightness temperature.

The DDAS is a dual 8-bit 8085 based 10 MHz micro-computer based system using "Multi-Bus" busing scheme between boards. Except for one universal card, commercial cards were used in the system, with minor modifications. Figure 18 is a block diagram of DDAS and the instrumentation connected to it. Table 2 is a list of the cards, modules and instrumentation by part or model number. The following is a brief operational description of the components of DDAS.

Master Computer

The master computer board is an Intel iSBC 80/24 with private RAM and EPROM memory. Provisions are provided on this card for installing small Intel compatible A/D and D/A modules. The primary functions of the master computer board are:

1)   Format the received PBMR data and store it on the common memory board.

2)   Compute the real-time display of the brightness temperature of each of the four channels.

3)   Convert the four beam brightness temperatures into digital values to drive the strip chart recorder. The strip chart recorder gives the operator, during the flight, a hardcopy presentation of brightness temperature variations over the data run for comparison. Offset and temperature range on the recorder is user-selectable under keyboard control.

4)   Read the PRT-5 infared radiometer and sweep angle through the A/D module.

5)   Act as system controller.

Slave Computer

The slave computer board is also a Intel 80/24 board, but configured to operate in the slave mode. Its primary functions are:

1)   Read the Loran-C navigational parameters over the asynchronous serial RS232C link operating at a nonstandard 19688 baud. Included in the data are position (latitude, longitude), ground speed, cross track error, and track angle. Format the data and merge it into the ping pong buffer on the common memory card using the pointer provided by the master computer. A time tick is included to synchronize with the complete time code read by the master computer.

2)   Read the aircraft attitude information, roll and pitch, through the synchro to digital converters.

3)   Write the formated data to the tape recorder when directed by the master computer. In order to minimize the number of boards in the system the data was streamed on the recorder under software control.

Common Memory Board

An Intel iSBC 108A/116A Combination Memory and I/O Expansion Board is used for the ping pong data buffer and common I/O port for reading time code by the Master CPU.

Synchro to Digital Converter Board

A universal Multibus interface card is used to interface the synchro to digital converter to the computer system bus.

Monitor/Keyboard Interface Board

A multibus compatible monitor/keyboard board is required for the system display and keyboard interface. It has write only memory for maintaining and updating the monitor and a keyboard input buffer.

The completed radiometer assembly is shown in figure 19. The power supply and Digital Processor Subassemblies can be seen mounted exterior of the thermal enclosure (Digital Processor on the right). The DDAS is shown assembled for aircraft installation in figure 20.

Test Results

In this section the results of laboratory and flight testing will be presented in support of the performance specifications listed in table 1. These results will include verification of the radiometer loop response, linearity of the radiometer, and determination of the antenna characteristics required for the data inversion algorithm. In addition the results of flight tests comparing the PBMR data to that of an existing L-Band radiometer will be discussed.

As noted in section 2 the control loop of the radiometer was designed to exhibit a first-order closed-loop response with a rise time of 40 ms. The step response of the radiometer was measured by switching the input port between a matched load at room temperature (approximately 290K) and a matched load submersed in liquid nitrogen (approximately 77K). The step response for each radiometer control loop was measured and is shown in figure 21. It can be seen from the figure that all four radiometer loops did meet the design goal of 40 ms.

Another important parameter of the radiometer is linearity. That is the linearity of the duty cycle to changes in the input antenna temperature. The test fixture used to measure the linearity consists of a matched load submersed in liquid nitrogen (i.e., at 77K) and a variable attenuation at room temperature. The effective temperature at the output of the attenuator can be approximated by

$$T_o \approx a\ 77 + (1 - a)\ T_{Att}$$

where $o < a < 1$ and represents the "gain" of the attenuator. It should be noted that although fixed mismatch losses in the setup can be ignored since only relative changes in T_o with changes in "a" are of interest, any change in VSWR of the variable attenuator as the attenuation is changed will result in an error. The results of these linearity tests are shown in figure 22.

The results of the linearity testing as well as measurements of a matched load at approximately 77K and 290K (i.e. liquid Nitrogen and room temperature) were then used to calibrate the radiometer receivers (without antenna). Once the receivers are calibrated, an estimate of the sensitivity (ΔT) of the receiver can be determined by measuring the standard deviation of the output in terms of effective input temperature. The entire sensor was also calibrated using measurements of the sky temperature (approx. 5K) and microwave absorber (approx. 300K) suspended over the antenna. It should be noted that only preliminary testing of this procedure was performed, and it is not claimed to be an optimal calibration procedure. The average expected (from hardware performance specification) and measured ΔT for the receivers were 0.62 kelvin and 0.64 kelvin respectively, and for the entire sensor (including the antenna losses the expected and measured sensitivity was 1.18 and 1.02 kelvin.

The instrument verification and testing also included a flight test phase. This phase of testing included the comparison of data from the PBMR with measurements of an existing single beam radiometer (L-Band) at 1.4 GHz with similar beam characteristics, as well as with ground truth measurements. The existing radiometer has undergone extensive testing and can be considered a proven instrument. However, the "L-Band" radiometer has an integration time of approximately 1 second, RF bandwidth of 50 MHz and most importantly an elliptically polarized antenna. Yet allowing for the effects of these differences the existing "L-Band" radiometer can be used to provide a continuous comparison for the PBMR. If the "L-Band" data is to be used to

verify the PBMR, the effects of the different instrument performance characteristics should be mentioned. The RF bandwidth of the "L-Band" system is 50 MHz as opposed to the 25 MHz PBMR bandwidth. The wider "L-Band" RF bandwidth will manifest itself as an improved ΔT (and more susceptable to interference), this will not adversely affect the data comparison. The "L-Band" radiometer also has an integration time of approximately 1 second where the PBMR integration is 0.5 seconds. This will provide better "L-Band" ΔT and some smearing of "L-Band" data over rapidly changing targets (soil moisture) due to the more sluggish response.

Finally the difference in the antenna beam characteristic must be considered. The antenna patterns for the "L-Band" and center beam of PBMR are qualitatively similar 20° 3 dB beam widths. However, the "L-Band" system is elliptically polarized where the PBMR is horizontally polarized. Thus, antenna correction may be difficult over some targets. This will be addressed where applicable in the discussion of flight test results.

The PBMR and L-Band radiometer were installed in the Bomb Bay of a NASA P-3 aircraft (fig. 23). The PBMR is located in the forward position with the center beam bore sighted with the L-Band beam for direct comparison of data. A television camera (white cylinder forward of PBMR) and a 35 mm camera are also bore sighted with the center beam of the PBMR.

The first flight line to be discussed was over a stretch of land containing a very large variation in soil moisture. This area included some swampy regions, areas of ponding, dryer regions and areas of thick vegetation coverage. It was hoped that this high contrast flight line could be used to determine the required time offset between the L-Band and PBMR. It should be noted that this offset is due not only to bore sight error, but also to the difference in integraton time and recording method. That is the PBMR records a sample every 0.5 sec which represents the measured scene for the preceding 0.5 sec, however, the L-Band records a sample every 0.3 sec which represents the preceding 1.0 sec (approximately) of data.

The PBMR and L-Band data for this flight line are shown in figure 24. Also shown in this figure is the cross correlation of PBMR and L-Band data, note the 0.25 sec offset in the peak. This offset corresponds to the PBMR data leading the L-Band by only one-half of a PBMR integration period, and was considered acceptable. Note the extremely high correlation between the data sets.

The data from the second flight line to be discussed are shown in figure 25. Note the low antenna temperatures over water and the sharp increase as the radiometer beams passed over the beach onto land. The scatter plot shown in the figure illustrates that the PBMR is responding linearly to the changes in target antenna temperature. The bias offset noticed between the L-Band and PBMR is due to the fact that the antenna correction algorithm mentioned earlier had not yet been performed.

The next test was to verify the antenna pattern correction algorithm developed from antenna chamber measurements. The incidence angle of the radiometer beams were varied by banking the aircraft at ±33° over the same target. Figure 26 shows a composite of data from the three beams at different incidence angles. The uncorrected values, i.e., data directly from the radiometer show the decrease in T_A with incidence angle which would be expected due to the horizonal polarization of the antenna. After applying the correction/inversion algorithm the effect of incidence angle are sufficiently compensated out to 35 to 40 degrees. The failure of the correction algorithm to perform properly at larger incidence angles is believed to be due to the cross polarization effect of the antenna that were ignored in the correction. That

is, although the antenna is designed to be horizontally polarized there is a small contribution to the received power which is vertically polarized, and since the power received from the surface which is vertically polarized increases with incidence angle out to 55° the effect of this cross polarization term would increase with incidence angle. The cross polarization pattern was measured and it is believed that if added to the correction algorithm, satisfactory correction could be performed at much larger incidence angles should it be required. It should be noted that the antenna correction algorithm was developed for a spectular surface of uniform brightness temperature (except for incidence angle dependence). While this is a reasonable assumption for the surface of water and salinity measurements, and indeed produced very good results, the use of this assumption for soil moisture where spatial dependence of brightness temperature may be large would likely not be valid. Finally, the brightness temperature measured by the PBMR and L-Band radiometer were compared to the predicted value as determined from ground truth measurements. The relationship between salinity, temperature, and incidence angle, the emissivity of sea water is fairly well understood. Further, since effects due to surface conditions are relatively small (compared to soil moisture measurement) in low wind/wave situations, it was determined that the Chesapeake Bay would be our location for the ground truth comparisons. Comparisons are made with the four ground truth samples.

The brightness temperature data for several flight lines made over the sea truth sites are shown in figures 27 through 30. The data shown is for the "L-Band" radiometer and the center beam of the PBMR. The data shown for each flight line is plotted versus time for approximately 30 seconds before and after the point closest to the sea truth vessel. Each point on the graph is an average of 5 seconds of radiometer data.

The radiometer data for three passes over sample site 1 are shown in figure 27. The brightness temperature calculated for sample 1 was 96.7K. Both radiometers are in relative agreement (i.e., within 2K) with this value. There also appears to be an increasing trend in the brightness temperature measured by both radiometers except for a jump of approximately 1K in the "L-Band" data for the last data run. The reason for this apparent shift in T_B for the "L-Band" radiometer is not known. It could be due to a rapid change in surface condition to which the horizontal polarized PBMR and elliptically polarized "L-Band" responded differently, although the time scale involved makes this seem unlikely. The measured T_B for sea truth sample #2 are shown in figure 28. Again, there is good agreement between the radiometer measurement and the sea truth sample. Figure 28 again shows an increase in T_B. This should not be considered error since the change in the scene brightness temperature was measured by both radiometers, the linear relationship between radiometers can be seen from the scatter plot. Data for sea truth samples 3 and 4 are shown in figures 29 and 30. Samples 3 and 4 were obtained from the south island of the Chesapeake Bay Bridge Tunnel, the large excursion in passes 2 and 3 of sample 3, and in sample 4 are due to the radiometers "seeing" the island. Thus, while these excursions should be excluded when comparing the data to sea truth sample, it is valid to use them when comparing data from the two radiometers. In fact the added dynamic range of T_B due to the partial beam fill of the island provides a wider range for this comparison.

The deviation of the measured T_B from the ground truth for both radiometers is demonstrated in the scatter plots (figs. 27 through 30) by the distance of each point from the origin. While this information is of interest and the agreement is quite good, the deviation includes errors in ground truth measurement and calculations. A more pertinent error from a radiometer system performance standpoint is the deviation from the "line of perfect agreement" (dotted line in figure). The mean, variance,

12

and rms value of this deviation are listed on the respective figures. These statistics include the calibration errors in both radiometers, stability errors in either of the radiometer, the effects of polarization on the measured brightness temperature, errors in the antenna correction algorithms, and measurement noise (ΔT) of both radiometers. Yet, the largest peak deviation from "perfect agreement" was 1.2K which occurred during sample 1 and the largest rms deviation of the four sites was 0.75K. Thus, even if all the difference between the "L-Band" and PBMR data is attributed to errors within the PBMR the absolute accuracy obtained at these four sites would still be within the design goal of 2K. Thus, the required accuracy was demonstrated in the actual aircraft environment.

CONCLUSIONS

The PBMR radiometer system was developed to demonstrate technologies that may be desirable in large-scale pushbroom applications, and to demonstrate the pushbroom concept in an aircraft prototype. The system was developed toward meeting the performance specification (see table 1) provided by GSFC such that, in addition to demonstrating the pushbroom imaging concept, the radiometer would be a valuable remote sensing instrument for soil moisture research.

The results of laboratory and flight testing of the PBMR presented above indicate that the radiometer does meet the performance specifications given by GSFC for soil moisture measurement. The instrument has been used in several joint LaRC/GSFC/USDA soil moisture flight experiments in Virginia, Texas, and California. The PBMR data from those experiments are being used to modify, develop and verify the algorithms used to predict soil moisture from remote sensing measurements. The image data obtained from those flights may also be useful in the study of the effects of beam characteristics on radiometer imaging data. This would be extremely useful since overly stringent antenna specifications may be far too costly or totally unattainable for the large space antenna systems that will produce the spatial resolution from orbit desired by soil moisture researchers. It then becomes important to more completely characterize the effects of antenna performance on the quality of radiometric soil moisture imaging data. Although it is beyond the scope of this paper, a study using theoretical models and PBMR images to quantitatively link spatial antenna characteristics to the accuracy of radiometric soil moisture image data would be extremely beneficial and is suggested as a future area of research.

Thus, in addition to the demonstration of possible pushbroom technologies, the PBMR is a useful remote sensing tool and engineering "test-bed" for radiometric research.

The far-field radiation pattern for each beam of the array was measured in an anechoic chamber with all other beam input ports terminated in 50 ohm loads. These pattern data are presented in figures A-1 through A-15 at 1413 MHz. The measurement coordinate system was such that the normal to the array points in the PHI = 0, THETA = 90° direction (i.e. the array is in the yz-plane with the electric field polarization in the z-direction). The E-plane (i.e. along-track) pattern for the center beam of the 3-beam configuration is shown in figure A-1 and the H-plane (i.e. cross-track) patterns for beams 1, 2, and 3 are presented in figures A-2, A-3, and A-4. The sidelobes for the center beam (number 2) are nominally around -23dB as is typical of a cosine amplitude distribution; however, the sidelobes nearest the array normal for beams 1 and 3 have increased as is typical of a phased array scanned away from broadside. The crossover level of the 3-beam configuration in the cross-track direction is about -9dB. Figures A-5 through A-8 show the H-plane (i.e. cross-track) patterns for beams 1-4 of the 4-beam configuration. The sidelobes for the 4-beam configuration are higher due to the uniform amplitude distribution. The beamwidth for the 4-beam configuration is narrower and the crossover level of thebeams has increased to about -4dB in the cross-track direction. Contour patterns for both configurations are presented in figures A-7 through A-15 for each beam.

REFERENCES

1. Njoku, E. G., and P. E. O'Neill: Multifrequency Microwave Radiometer Measure-ments of Soil Moisture. IEEE Trans. Geoscience and Remote Sensing, GE-20 (4), pp. 468-475, 1982.

2. Burke, H.-H. K., and T. J. Schmugge: Effects of Varying Soil Moisture Contents and Vegetation Canopies on Microwave Emissions. IEEE Trans. Geoscience and Remote Sensing, GE-20 (3), pp. 268-273, 1982.

3. NASA Lyndon B. Johnson Space Center: Skylab EREP Investigations Summary. NASA Special Publication 399, Washington, DC, 1978.

4. Blume, H.-J. C., B. M. Kendall, and J. C. Fedors: Sea Surface Temperature and Salinity Mapping from Remote Microwave Radiometric Measurements of Brightness Temperature. NASA Techn. Paper 1077, Langley Research Center, Hampton, VA, 1977.

5. Bernstein, R. L., and J. H. Morris: Tropical and Mid-Latitude North Pacific Sea Surface Temperature Variability from the SEASAT SMMR. J. Geophys. Res. 88 (C3), pp. 1877-1891, 1983.

6. Gleorsen, P.: Sea Surface Temperatures from Nimbus-7 SMMR Radiances, J. Climate and Applied Meteorology, 23, pp. 336-340, 1984.

7. Blume, H.-J. C., B. M. Kendall, and J. C. Fedors: Multifrequency Radiometer Detection of Submarine Freshwater Sources Along the Puerto Rican Coastline. J. Geophys. Res. 86 (C6), pp. 5283-5291, 1981.

8. Kendall, B. M., and J. O. Blanton: Microwave Radiometer Measurement of Tidally Induced Salinity Changes off the Georgia Coast. J. Geophys. Res. 86 (C6),pp. 6435-6441, 1981.

9. Jones, W. L., P. G. Black, V. E. Delnore, and C. T. Swift: Airborne Microwave Remote-Sensing of Hurricane Allen. Science, 214, pp. 274-280, 1981.

10. Swift, C. T., W. L. Jones, Jr., R. F. Harrington, J. C. Fedors, R. H. Couch, and B. L. Jackson: Microwave Radar and Radiometric Remote Sensing Measurements of Lake Ice. Geophys. Res. Letters, 7 (4), pp. 243-246, 1980.

11. Cavalieri, D. J., P. Gloersen, and W. J. Campbell: Determination of Sea Ice Parameters with the NIMBUS 7 SMMR. J. Geophys. Res., 89 (D4), pp. 5355-5369, 1984.

12. Schanda, E., C. Matzler, and K. Kunzi: Microwave Remote Sensing of Snow Cover. Int. J. Rem. Sensing, 4 (1), pp. 149-158, 1983.

13. Kunzi, K. F., S. Patil, and H. Rott: Snow-Cover Parameters Retrieved from Nimbus-7 Scanning Multichannel Microwave Radiometer (SMMR) Data. IEEE Trans. Geoscience and Remote Sensing, GE-20 (4), pp. 452-467, 1982.

14. Alishouse, J. C.: Total Precipitable Water and Rainfall Determinations from the SEASAT Scanning Multichannel Microwave Radiometer. J. Geophys. Res., 88 (C3), pp. 1929-1935, 1983.

15

15. Takeda, T., and S. Natsuki: Estimation of Liquid Water Amount in an Extended Cloud by Nimbus-5 Microwave Data. J. Met. Society of Japan, 60 (5), pp. 1153-1164, 1982.

16. Prabhakara, C., H. D. Chang, and A. T. C. Chang: Remote Sensing of Precipitable Water over the Oceans from Nimbus 7 Microwave Measurements. J. Appl. Met., 21, pp. 59-67, 1982.

17. Susskind, J., J. Rosenfield, D. Reuter, and M. T. Chahine: Remote Sensing of Weather and Climate Parameters from HIRS2 MSU on TIROS-N. J. Geophys. Res., 89 (D3), pp. 4677-4697, 1984.

18. Blume, H.-J. C., A. W. Love, M. J. vanMellen, and W. H. Ho: Radiometric Observations of Sea Temperature at 2.65 GHz over the Chesapeake Bay. IEEE Trans. Antennas and Propagation, AP-25 (1), pp. 121-128, 1977.

19. Harrington, R. F.: The Development of a Stepped Frequency Microwave Radiometer and its Application to Remote Sensing of the Earth. NASA TM-81847, Langley Research Center, 1980.

20. NORSEX Group: Norwegian Remote Sensing Experiment in a Marginal Ice Zone, Science, 220 (4599), pp. 781-787, 1983.

21. Harrington, R. F.: C-Band Stepped Frequency Radiometry for Hurricane Probing. Presented at 1981 IEEE International Geoscience and Remote Sensing Symposium, June 8-10, 1981, Washington, DC.

22. Keafer, L. S., Jr., and R. F. Harrington: Radiometer Requirements for Earth-Observation Systems Using Large Space Antennas. NASA Ref. Pub. 1101, Langley Research Center, Hampton, VA, 1983.

23. M. C. Bailey, "A Simple Stripline Design for Uneven Power Split", NASA Technical Memorandum 81870, August 1980.

16

TABLE 1

	3-Beam	4-Beam
Frequency		1413 MHz
Bandwidth		25 MHz
Integration Time		0.5 seconds
Sensitivity		1.0 kelvin
Accuracy		2.0 kelvin
Polarization		Horizontal
Resolution Cell*	290-570 ft	200 ft to 260 ft
Swath Width*	1400 ft	750 ft

*500 ft Altitude using 9 dB contour.

Table 2

1) <u>Intel iSBC 80/24</u> Single Board Computer Board

2) <u>Intel iSBC 80/24</u> Single Board Computer Board

3) <u>Intel iSBC 108A/116A</u> Combination Memory and I/D Expansion Board

4) Electronic Solution <u>Multi-Interface Board with</u> Analog Devices
       SDC 1742-411 Synchro to Digital Converter module

5) <u>Matrox Electronics Systems MSBC 3480</u> Monitor and Keyboard
       Interface Module

6) <u>Intel iSbX 311</u> Analog to Digital Multimodule Input Board

7) <u>Intel iSBX 328</u> Digital to Analog Multimodule Output Board

8) <u>Barnes Associates</u>, PRT-5 Infared Radiometer

9) <u>Push Broom Microwave Radiometer</u>, NASA Langley Research Center
       Instrument

10) <u>Soltec</u>, Model 3314, Strip Chart Recorder

11) <u>Datum</u>, Model 9100A, Time Code Generator

12) Video Monitor

13) ASC11 Keyboard

14) <u>Teledyne</u>, Model TDL-711 Loran-C Navigator

15) <u>Kennedy</u>, Model 9700 Digital Tape Recorder

16) presently not being used

17) <u>Collins</u> 332D-11(a) Vertical Reference
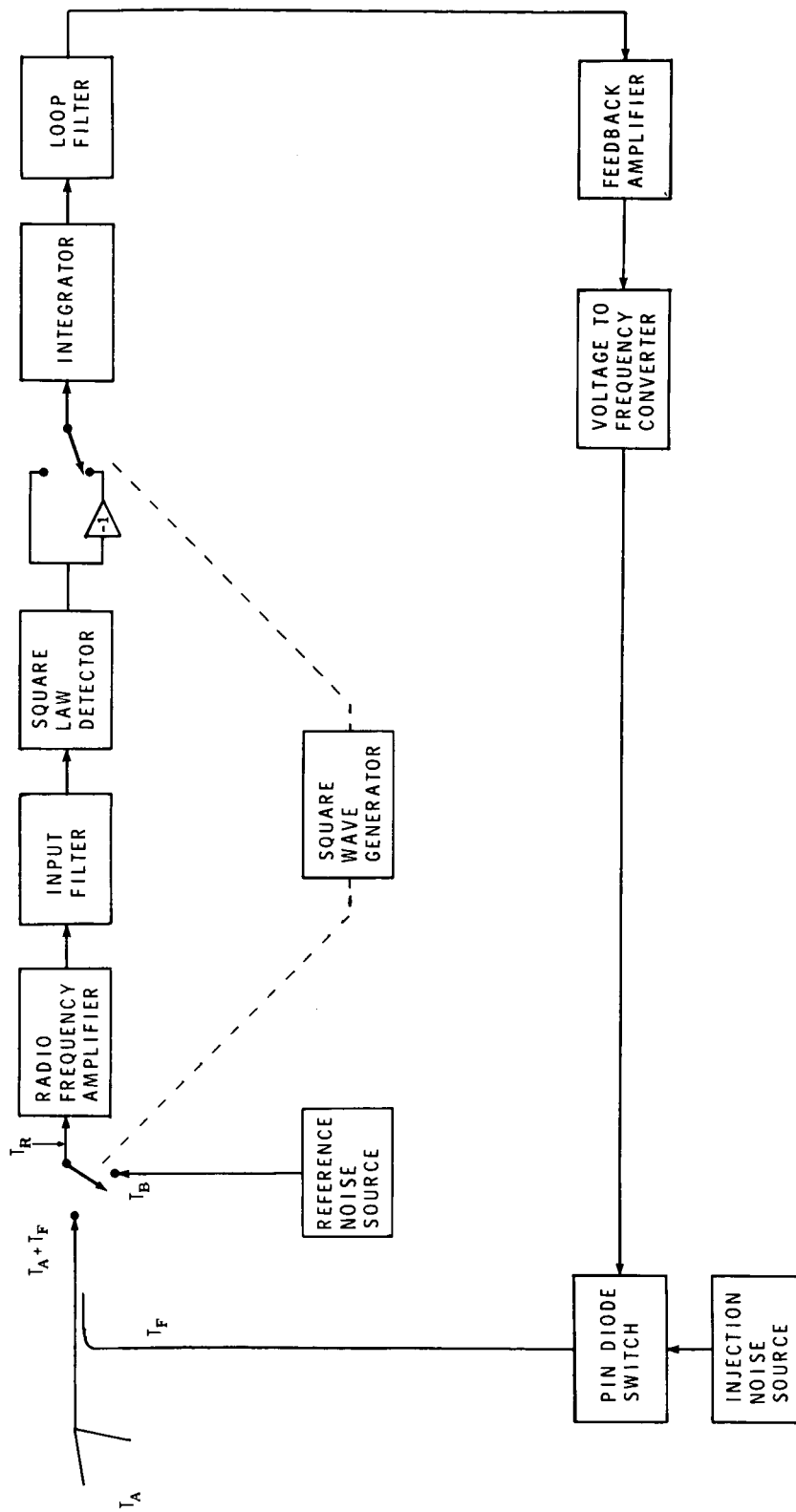
Figure 1.- Dicke switching noise injection radiometer.
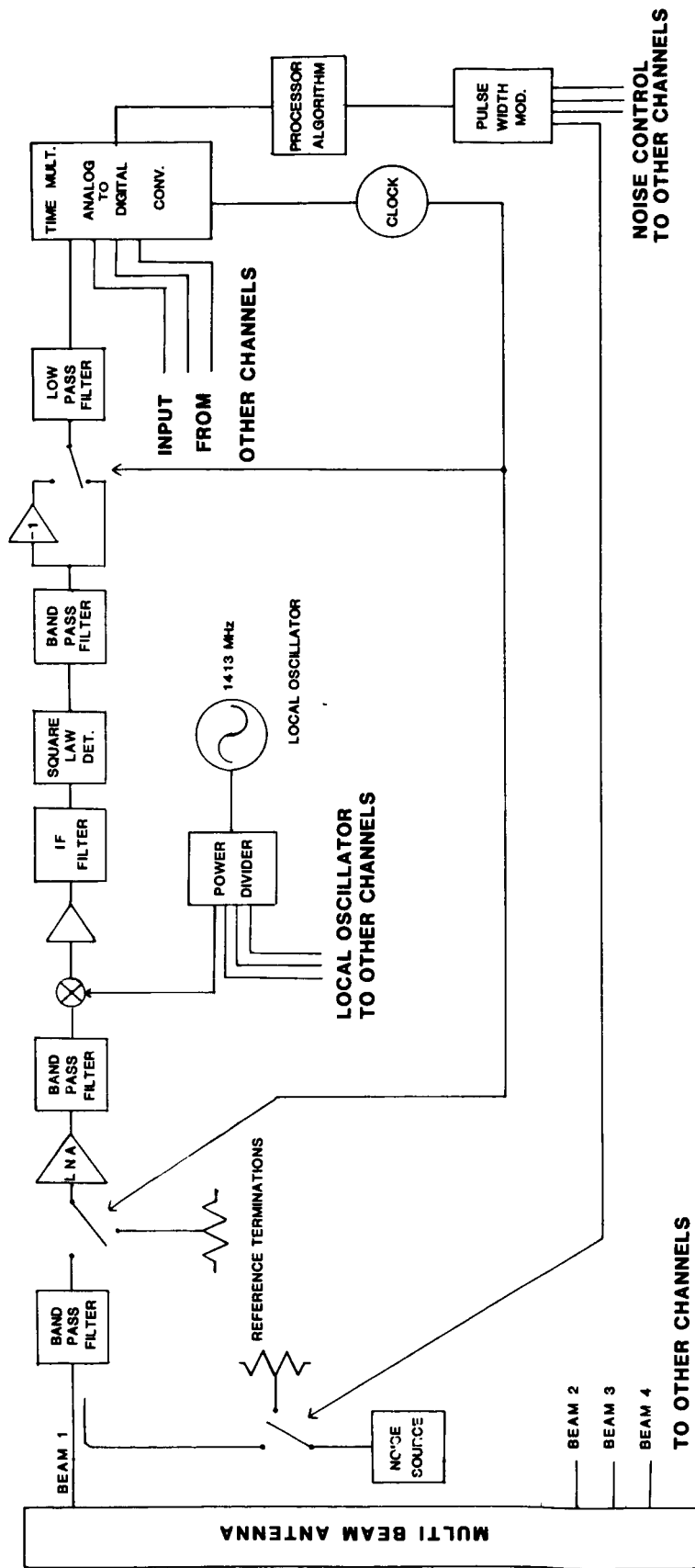
Figure 2.- Simplified PBMR block diagram.
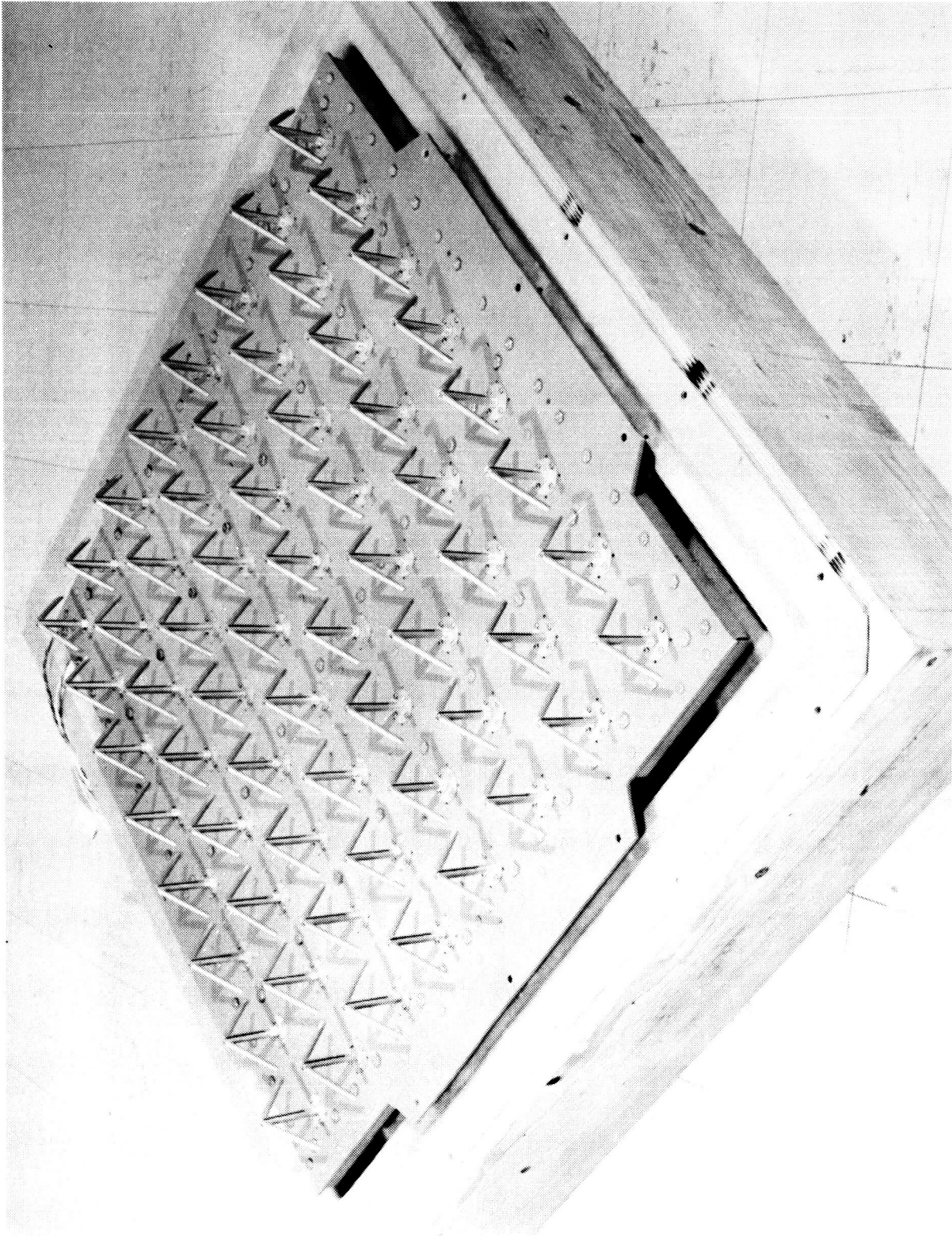
Figure 3.- Dipole array.
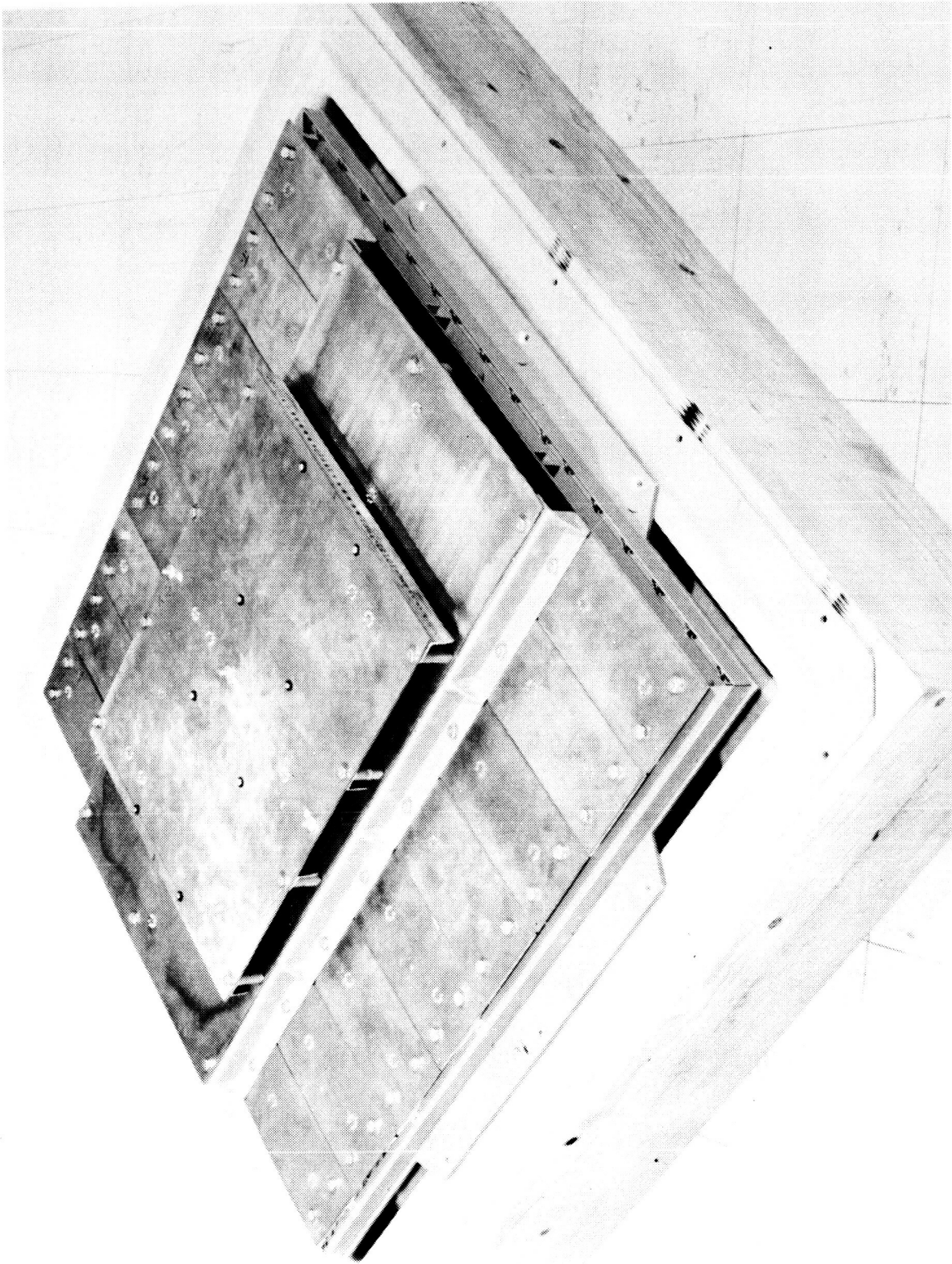
Figure 4.- Antenna feed network.
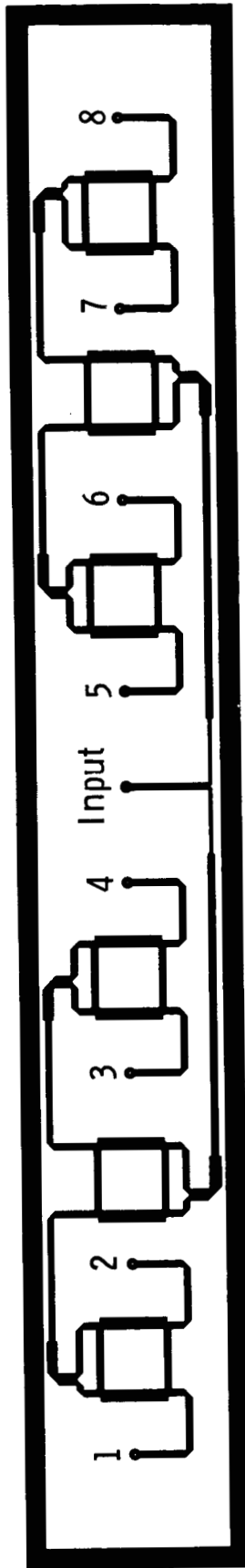
Figure 5.- Stripline circuit layout for 8-element cosine distribution.

23
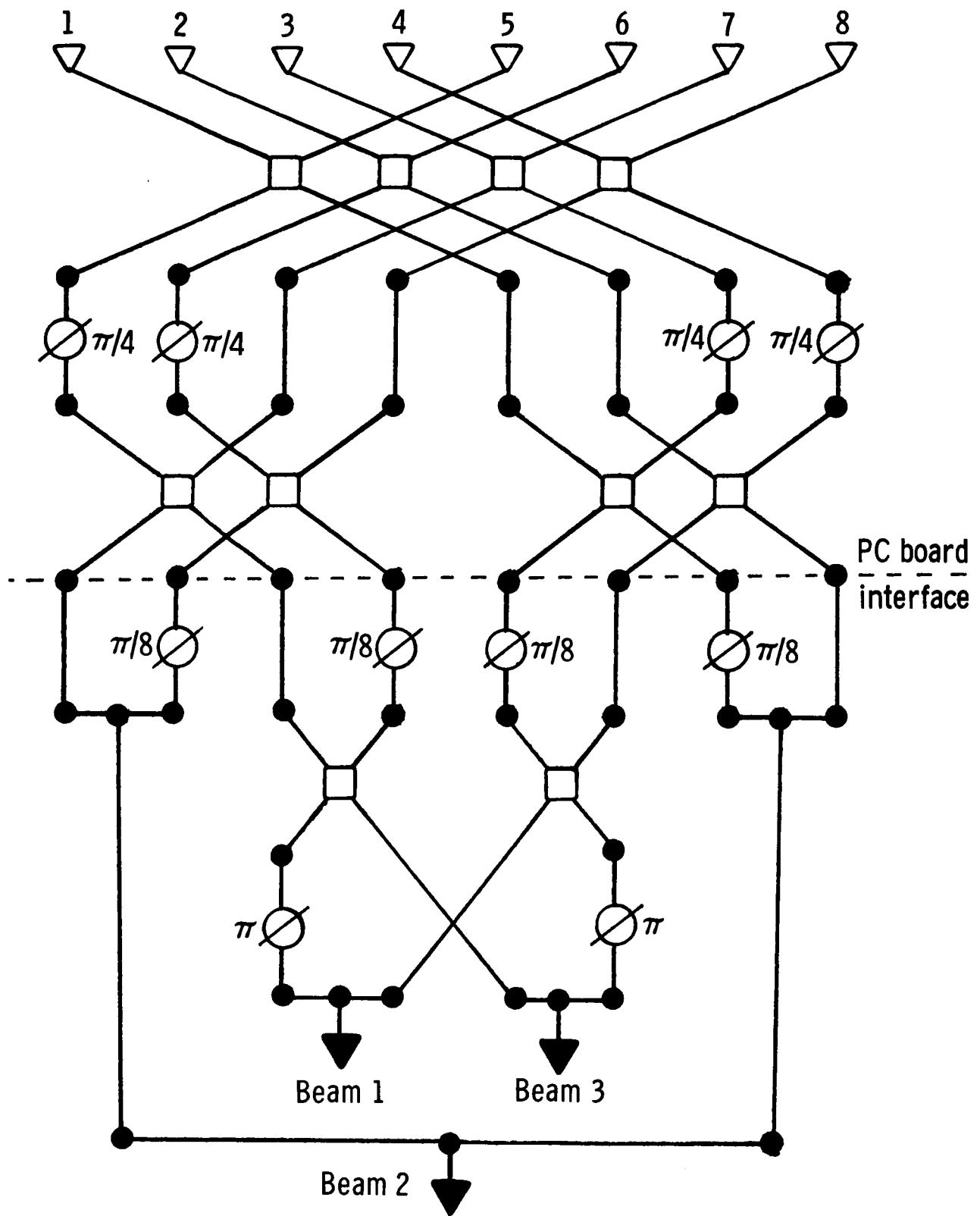
Figure 6.- Schematic of simultaneous 3-beam cosine amplitude tapered feed-network.

24
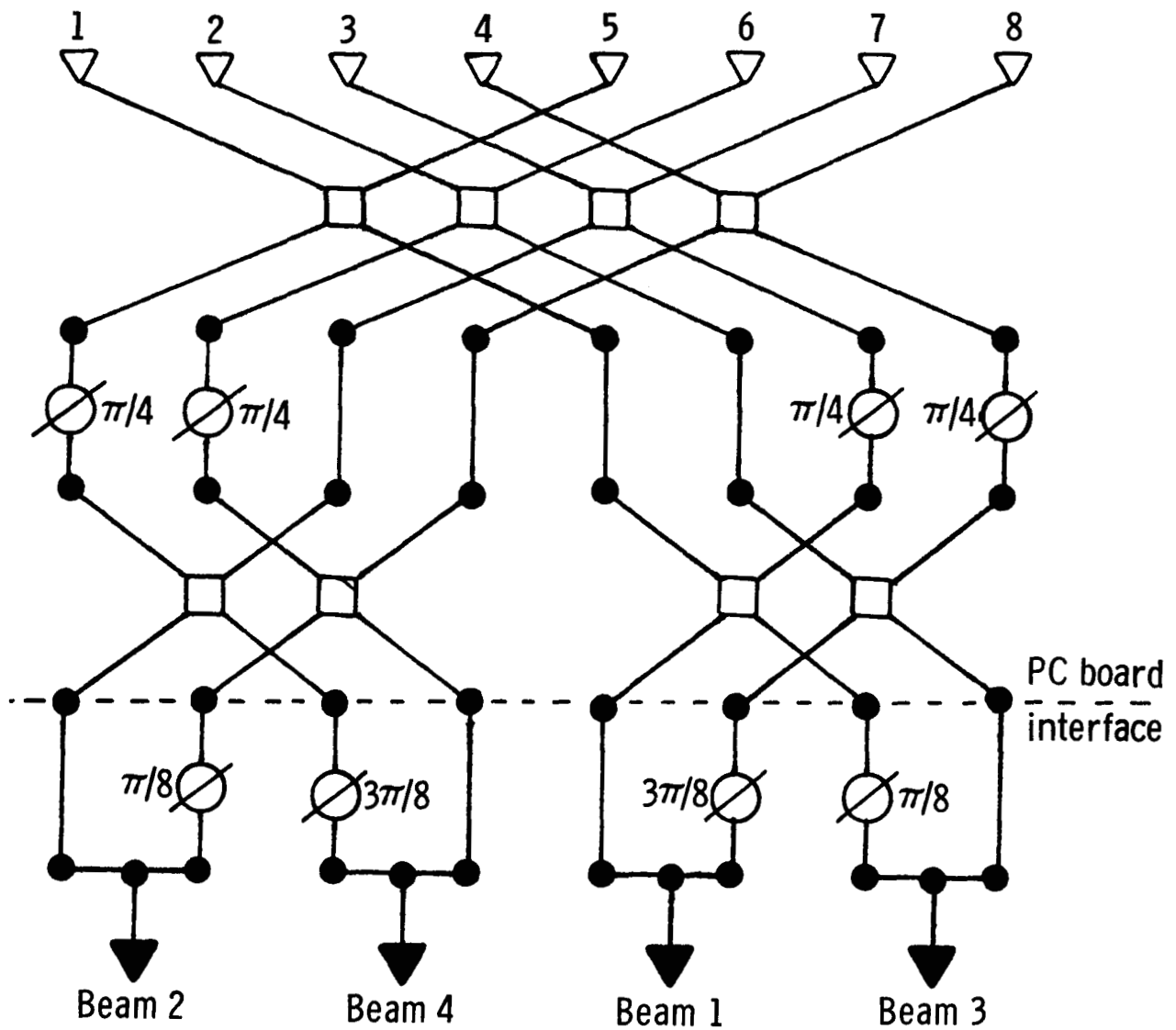
Figure 7.- Schematic of simultaneous 4-beam uniform amplitude-tapered feed-network.
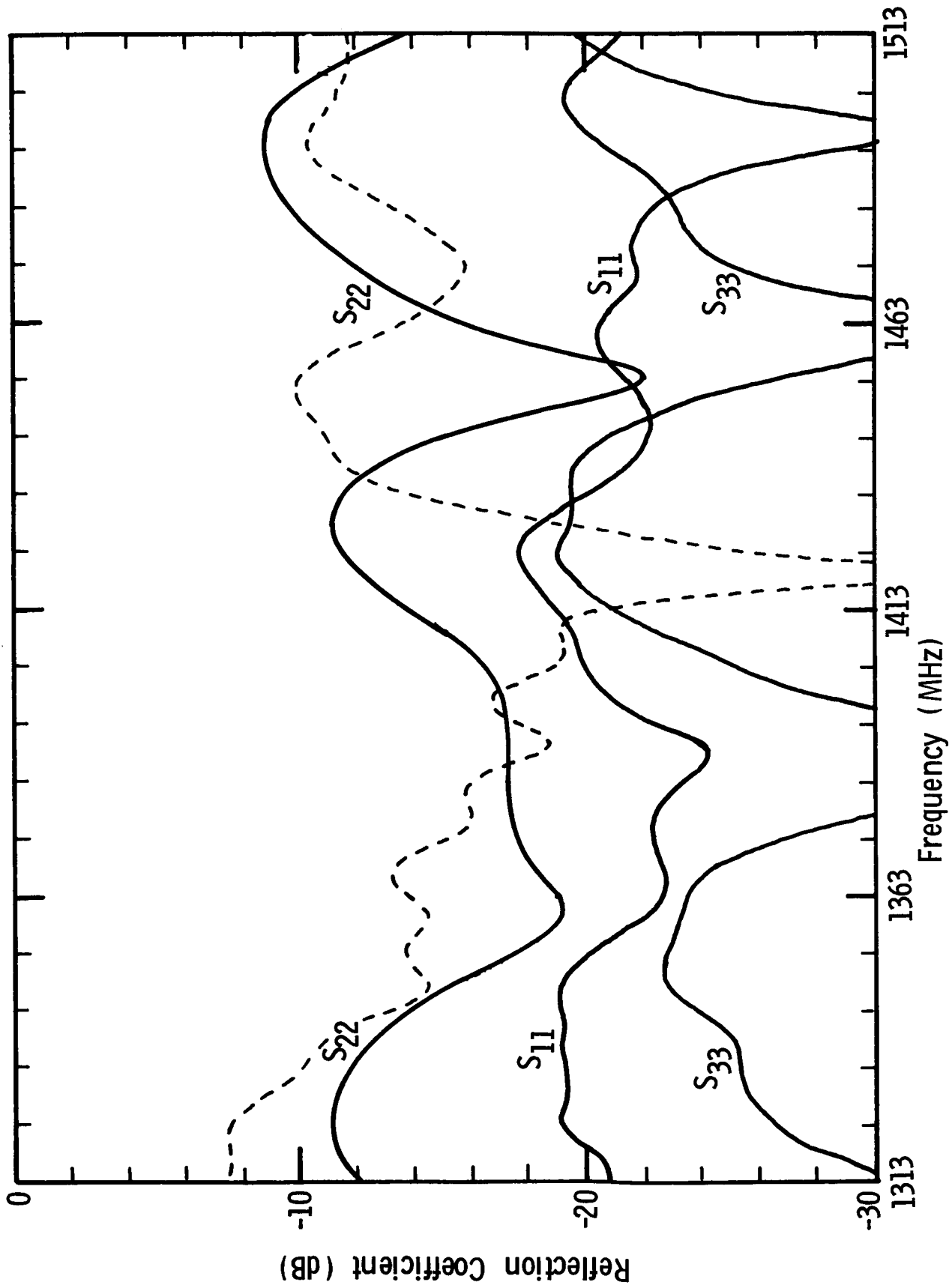
Figure 8.– Measured input reflection coefficient versus frequency for 3-beam antenna array.
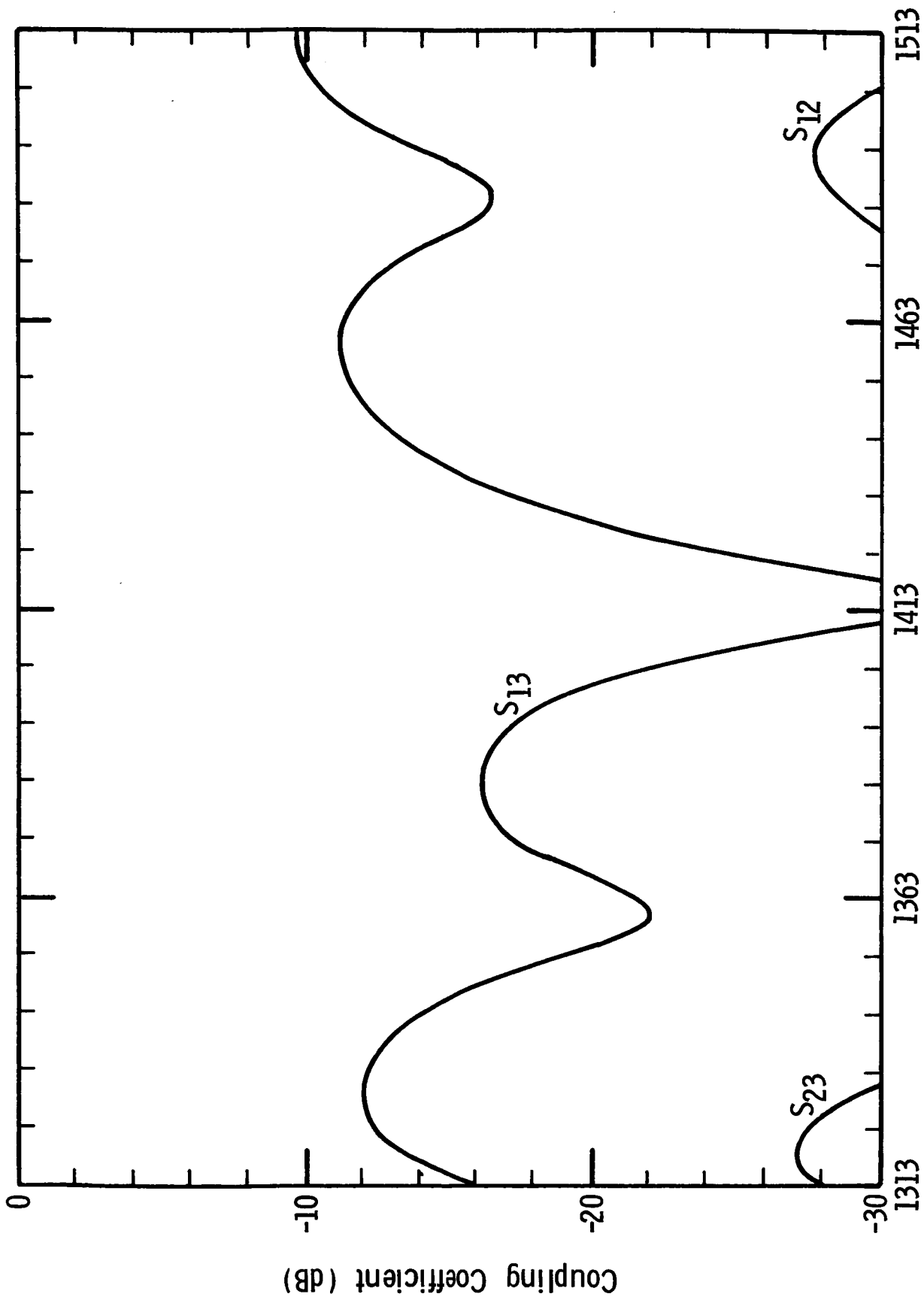
Figure 9.— Measured isolation between input ports versus frequency for 3-beam antenna array.
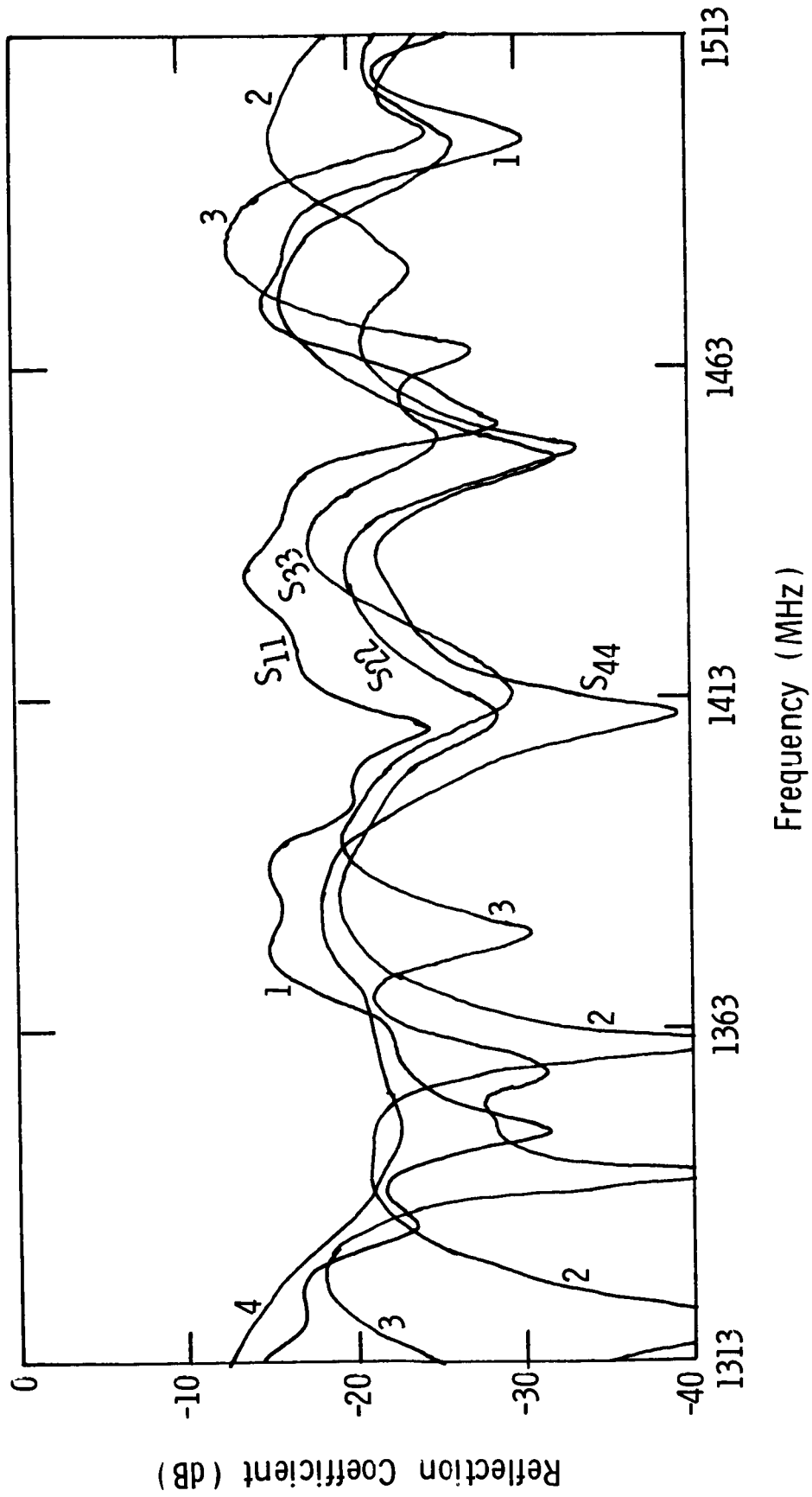
Figure 10.– Measured input reflection coefficient versus frequency for 4-beam antenna array.
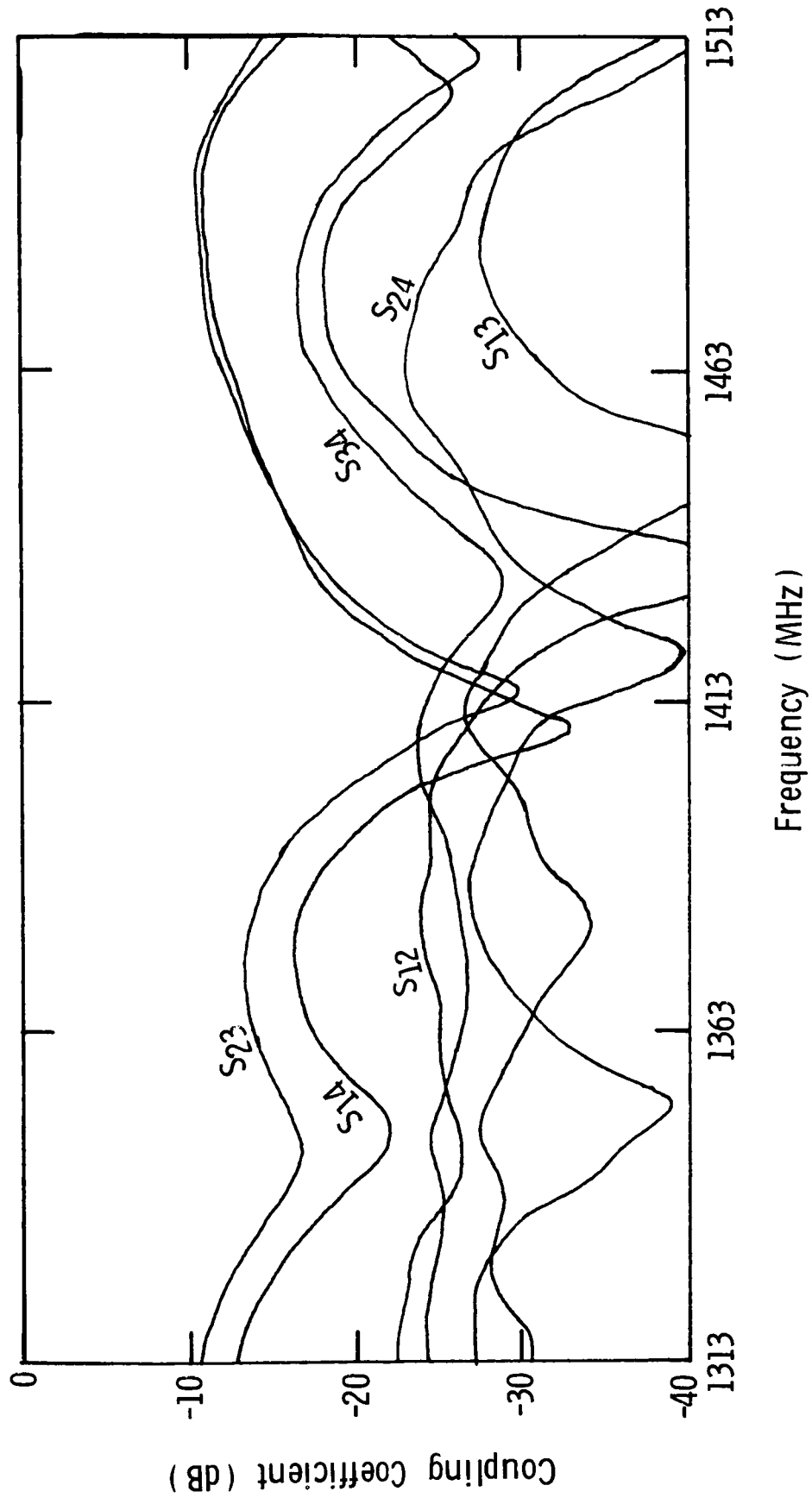
Figure 11.- Measured isolation between input ports versus frequency for 4-beam antenna array.

29
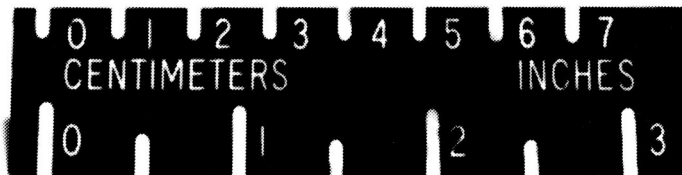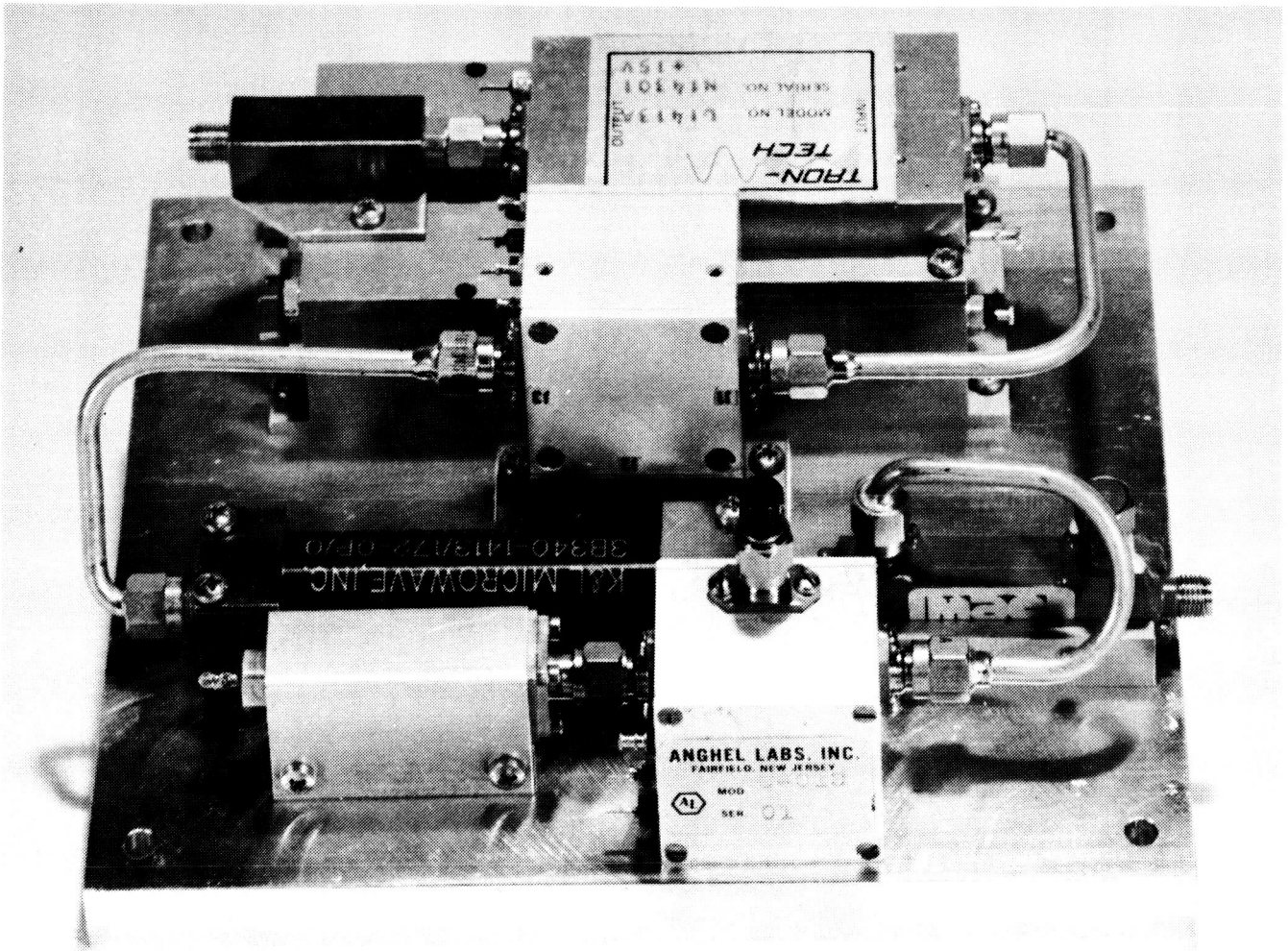
Figure 12.- Radiometer front-end assembly.
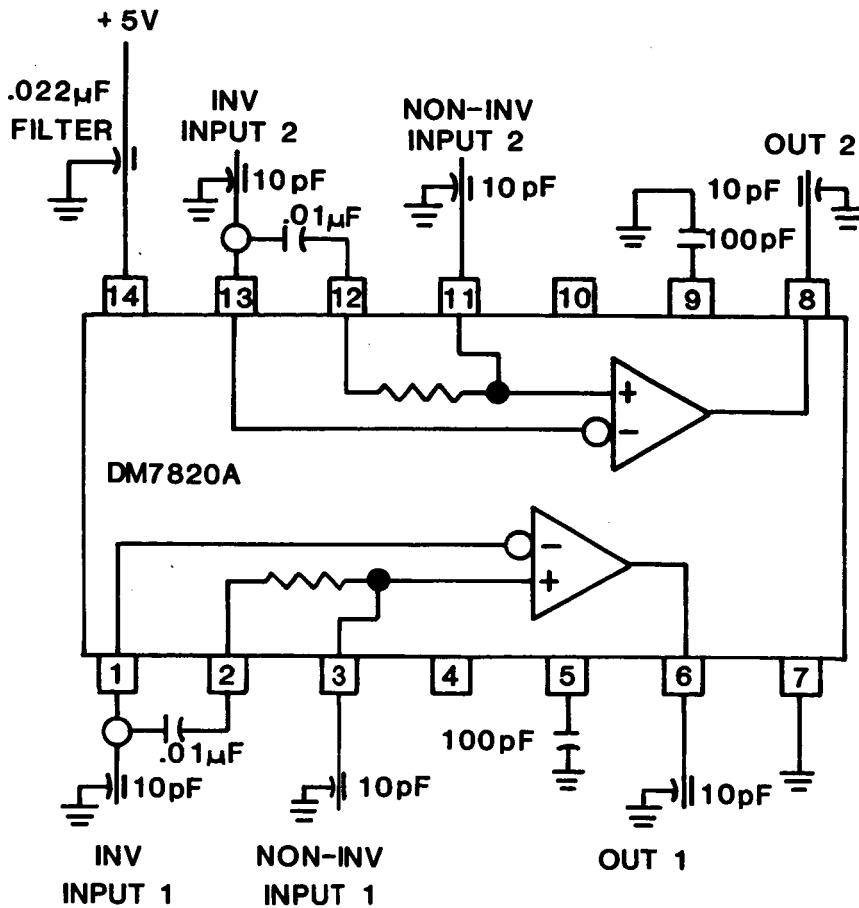
Figure 13(a).- Line receiver.
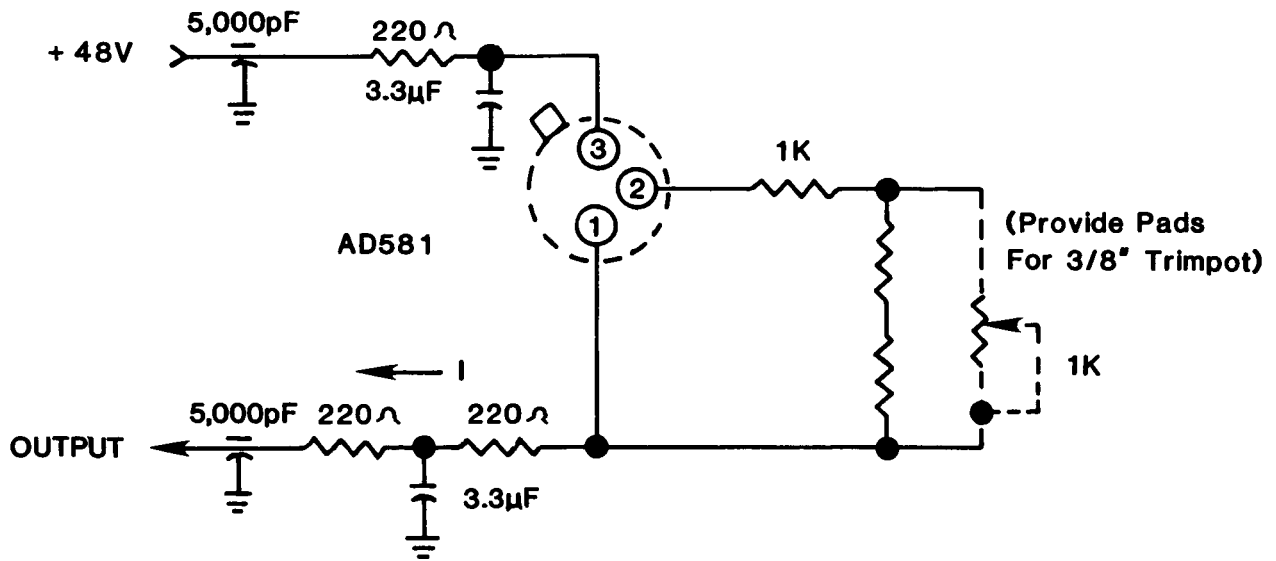
Figure 13(b).- Constant current source.
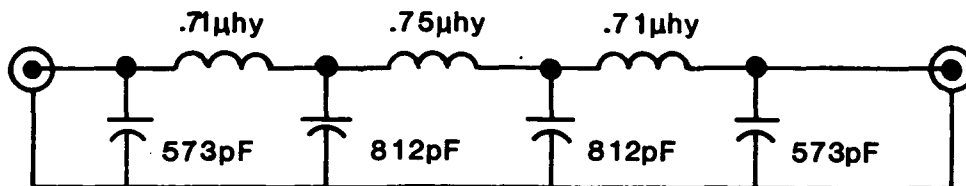
Measured Electrical Characteristics

Insertion loss   < 0.5 dB
Inband return loss > 10 dB
(V_p/V_v) -------   ≈ 1 dB
- 3dB bandwidth: 12.3 ± 0.1 MHz

Component Data

Capacitors: Selected ceramic "chip" types

     .71 μhy - 13T #26 on micrometals
              T30-7 form
     .75 μhy - 14T #24 on T30-7 form

Figure 14.- 12.5 MHz low pass filter.
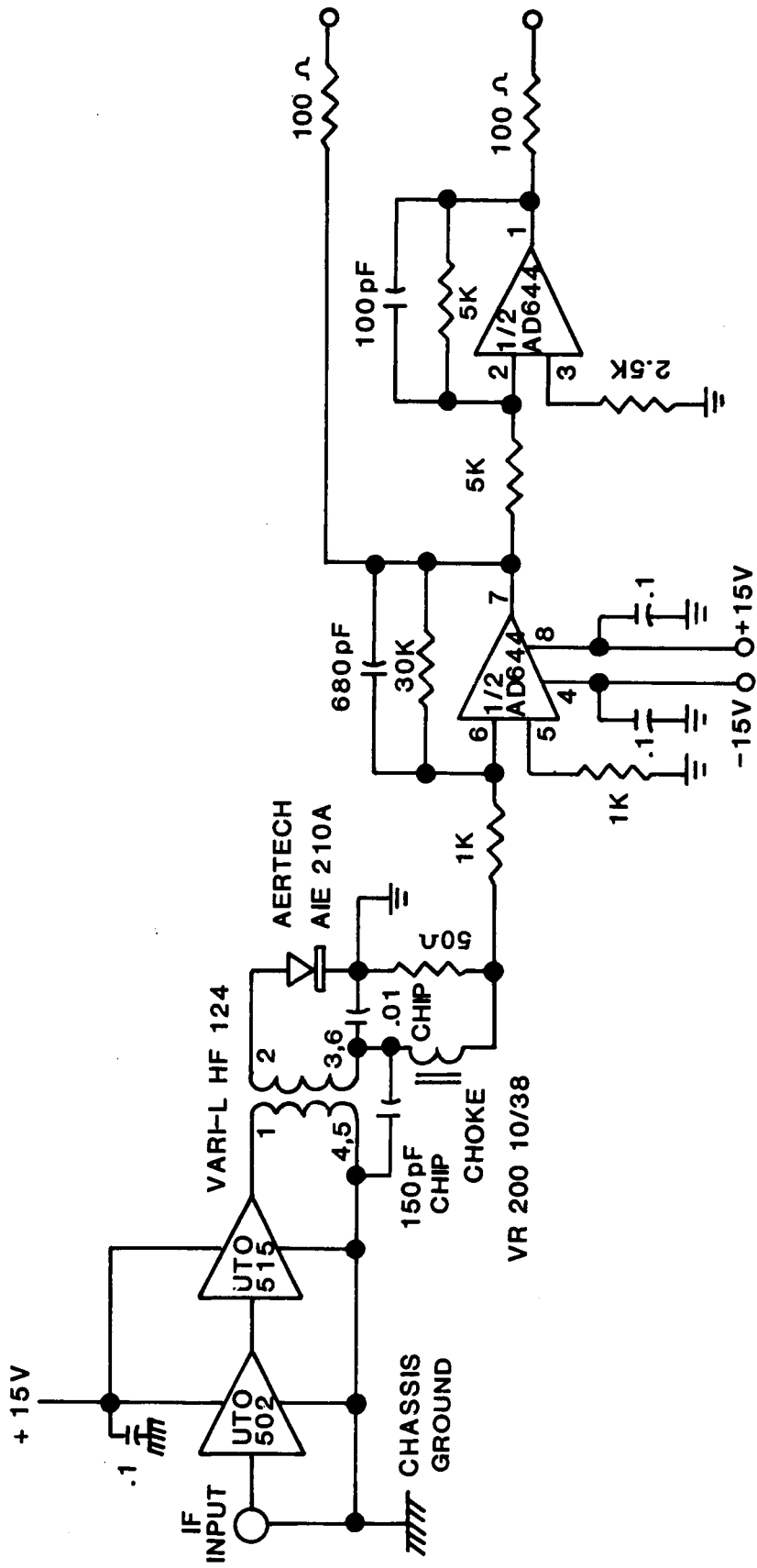
Figure 15.— Amplifier/square-law detector.
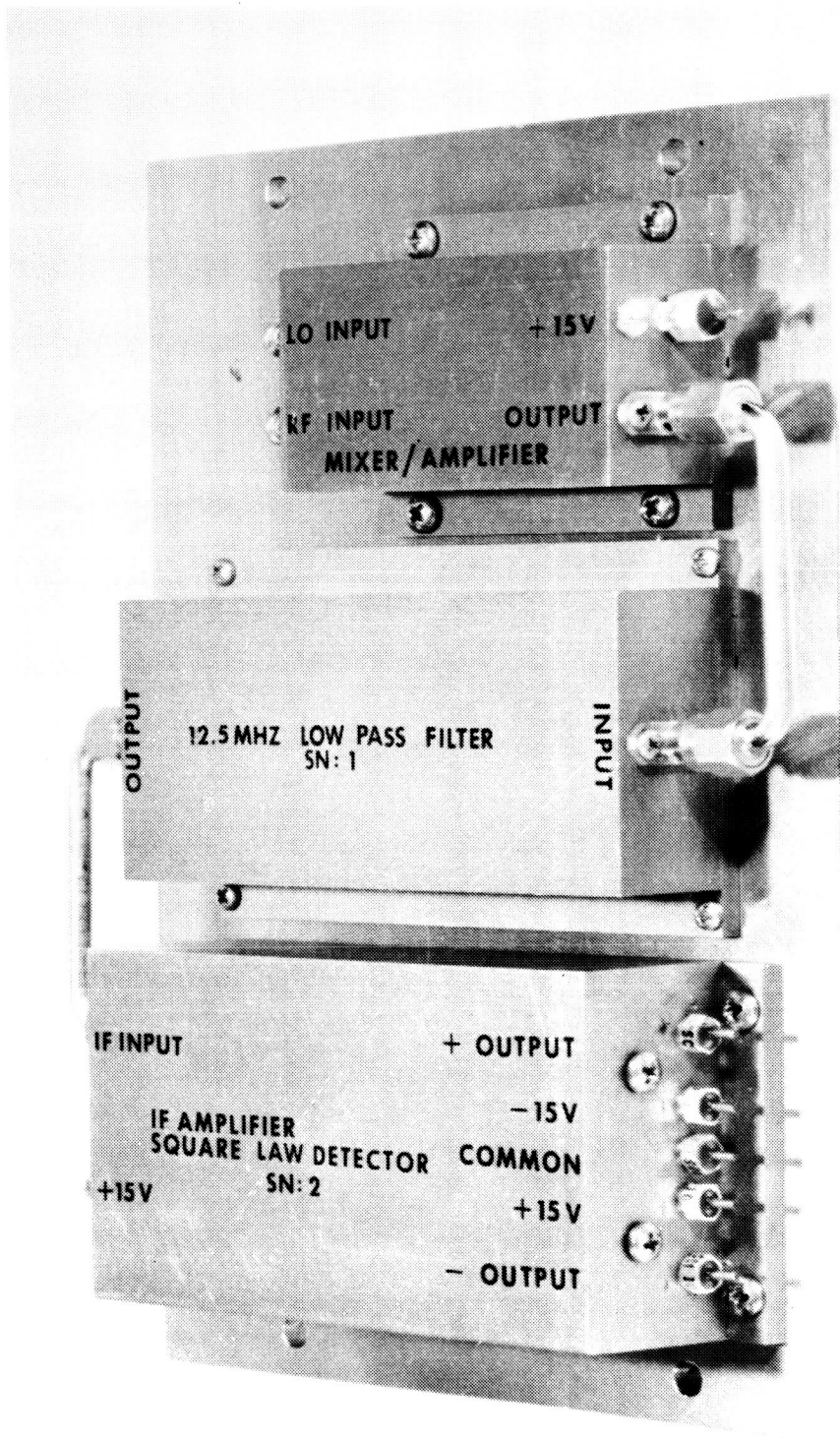
Figure 16.- IF assembly.
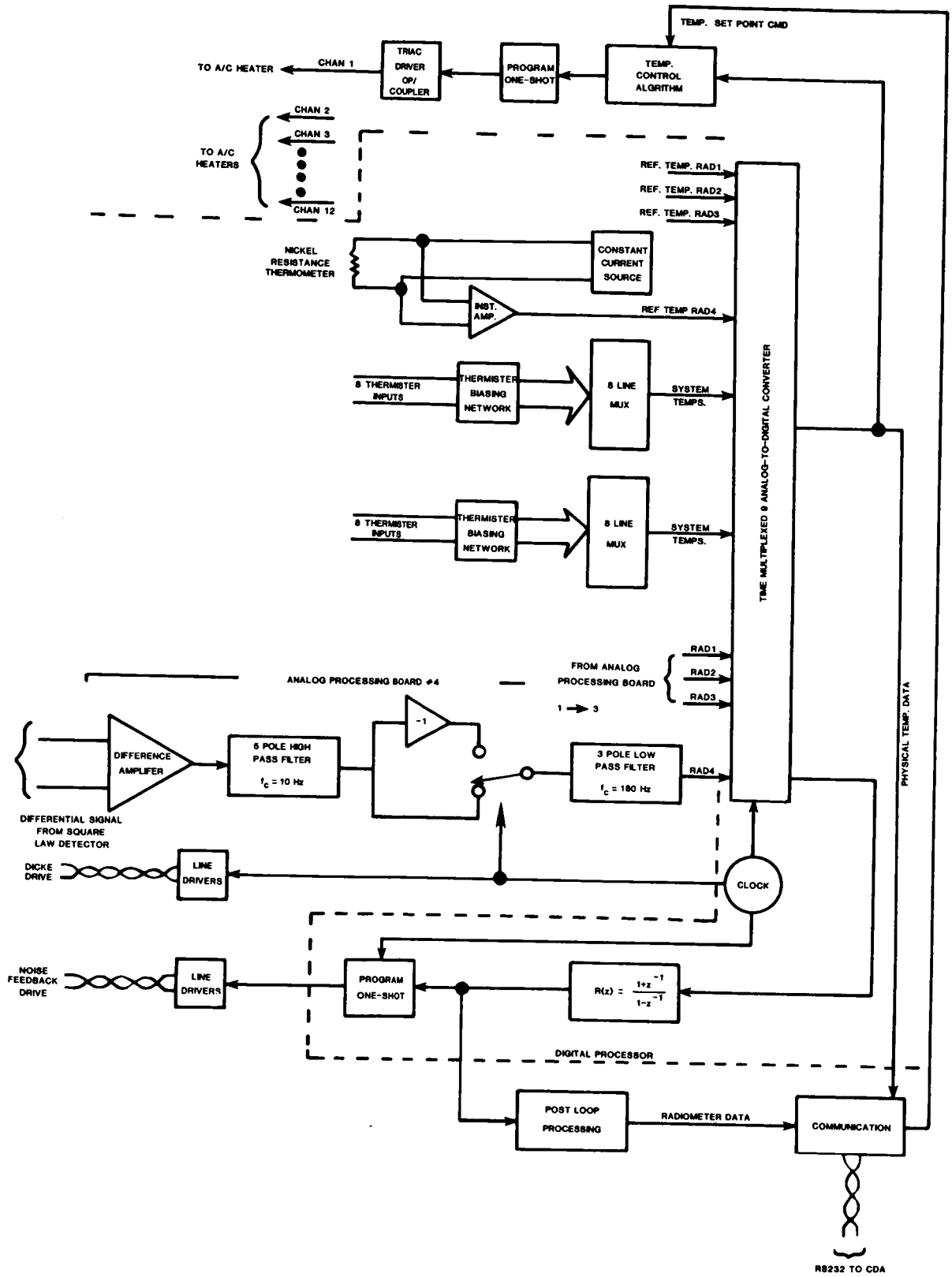
Figure 17.- Signal processing functional block diagram.
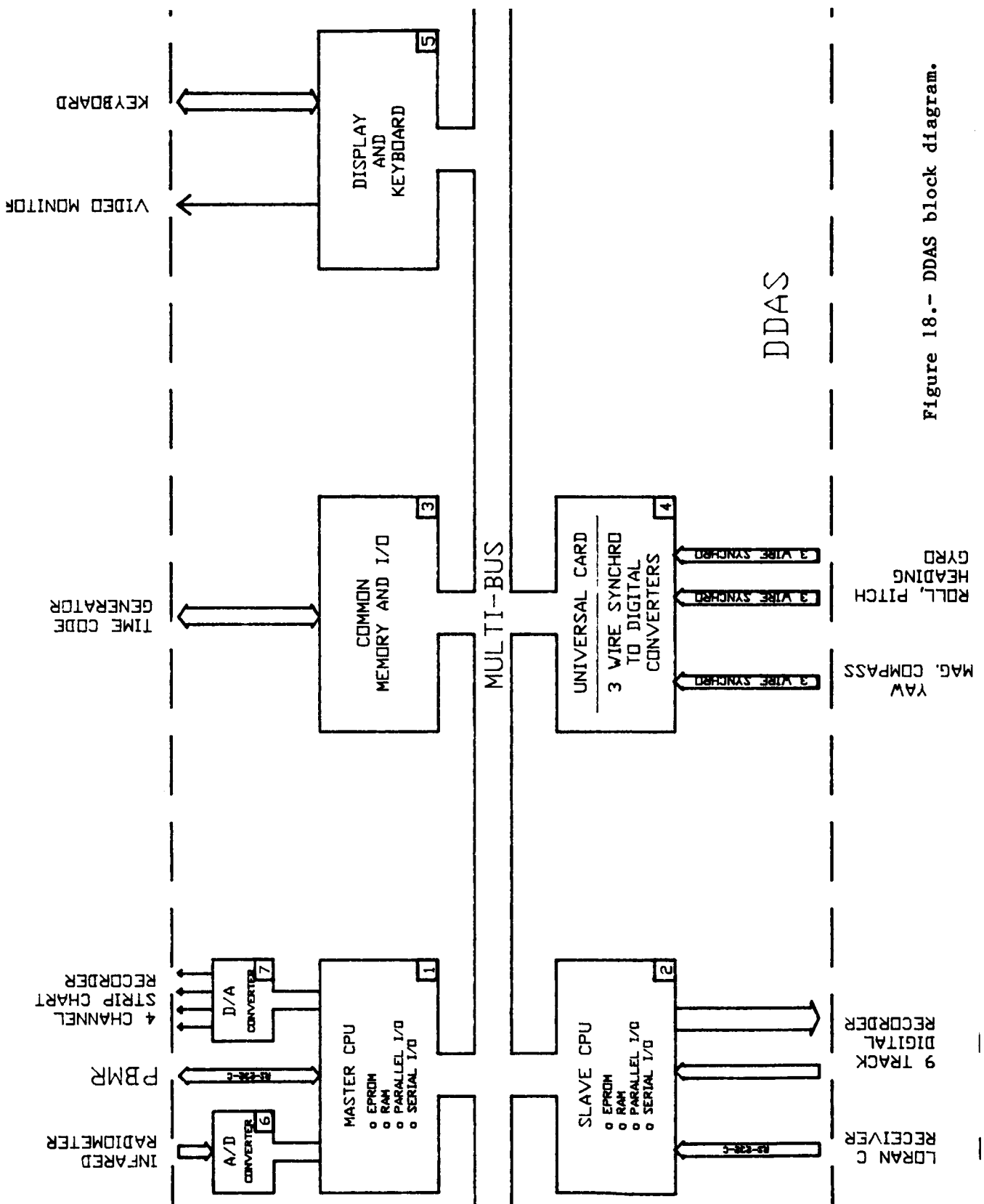
Figure 18.– DDAS block diagram.
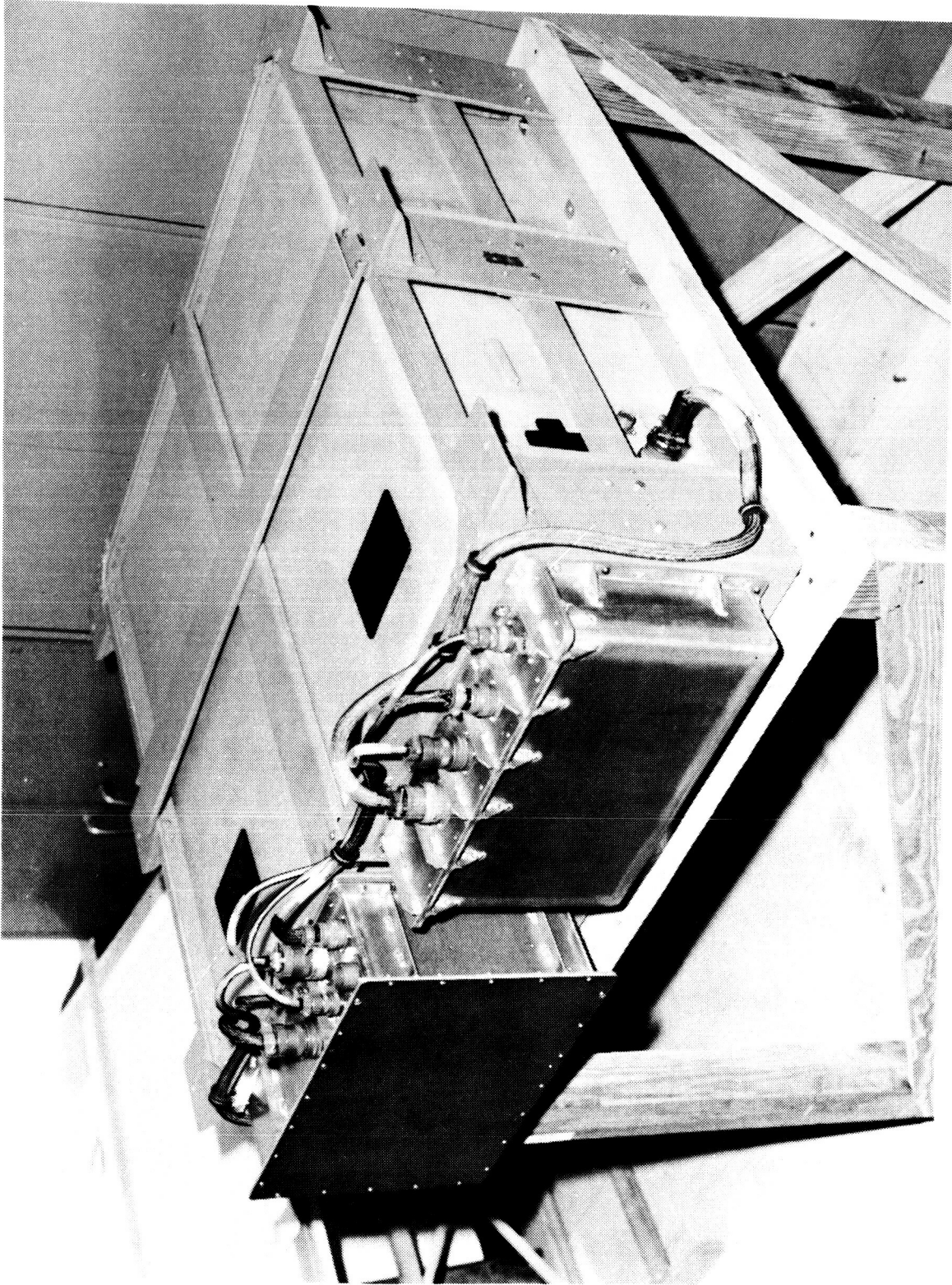
Figure 19.- PBMR radiometer assembly.
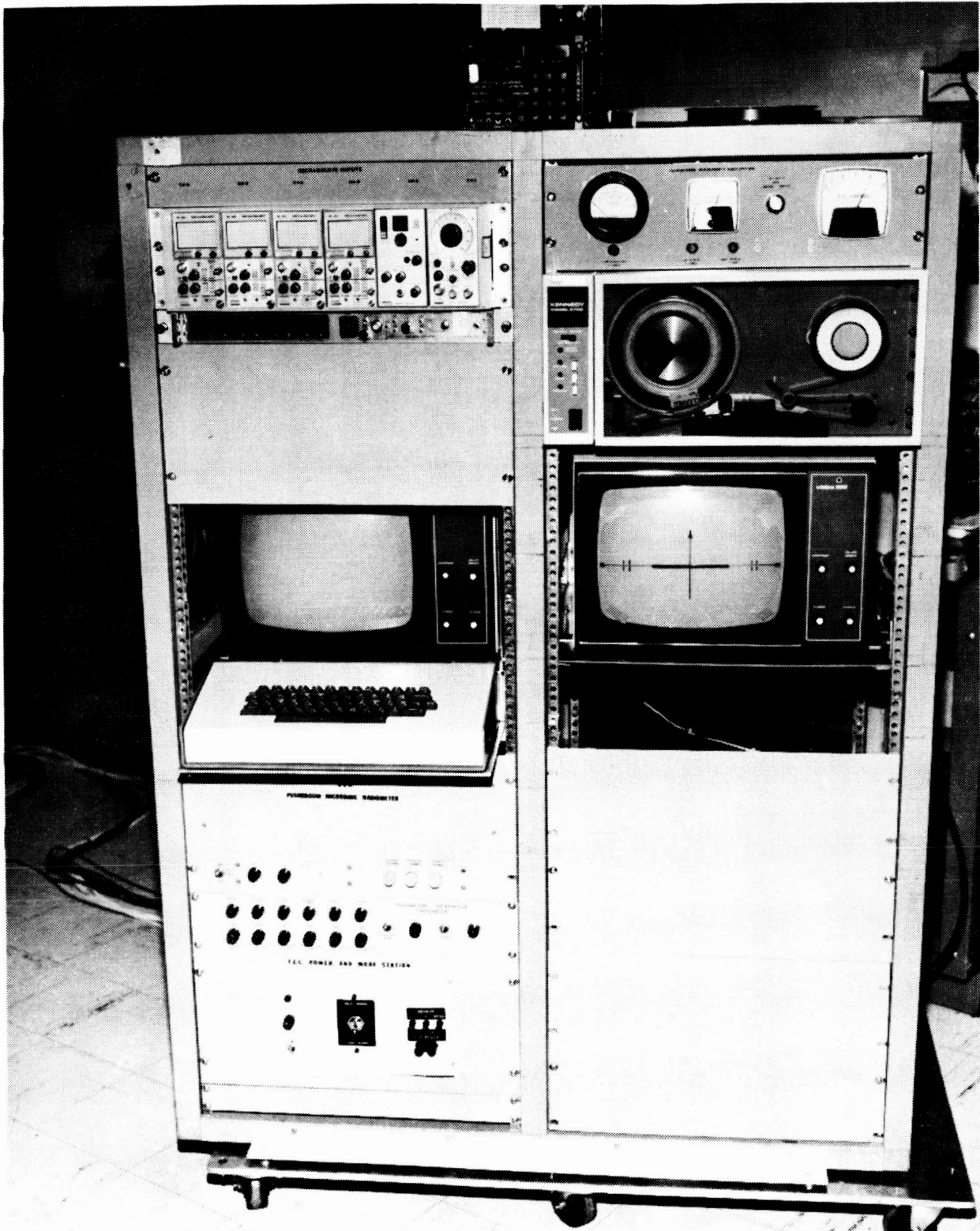
Figure 20.- PBMR display and data acquisition system.
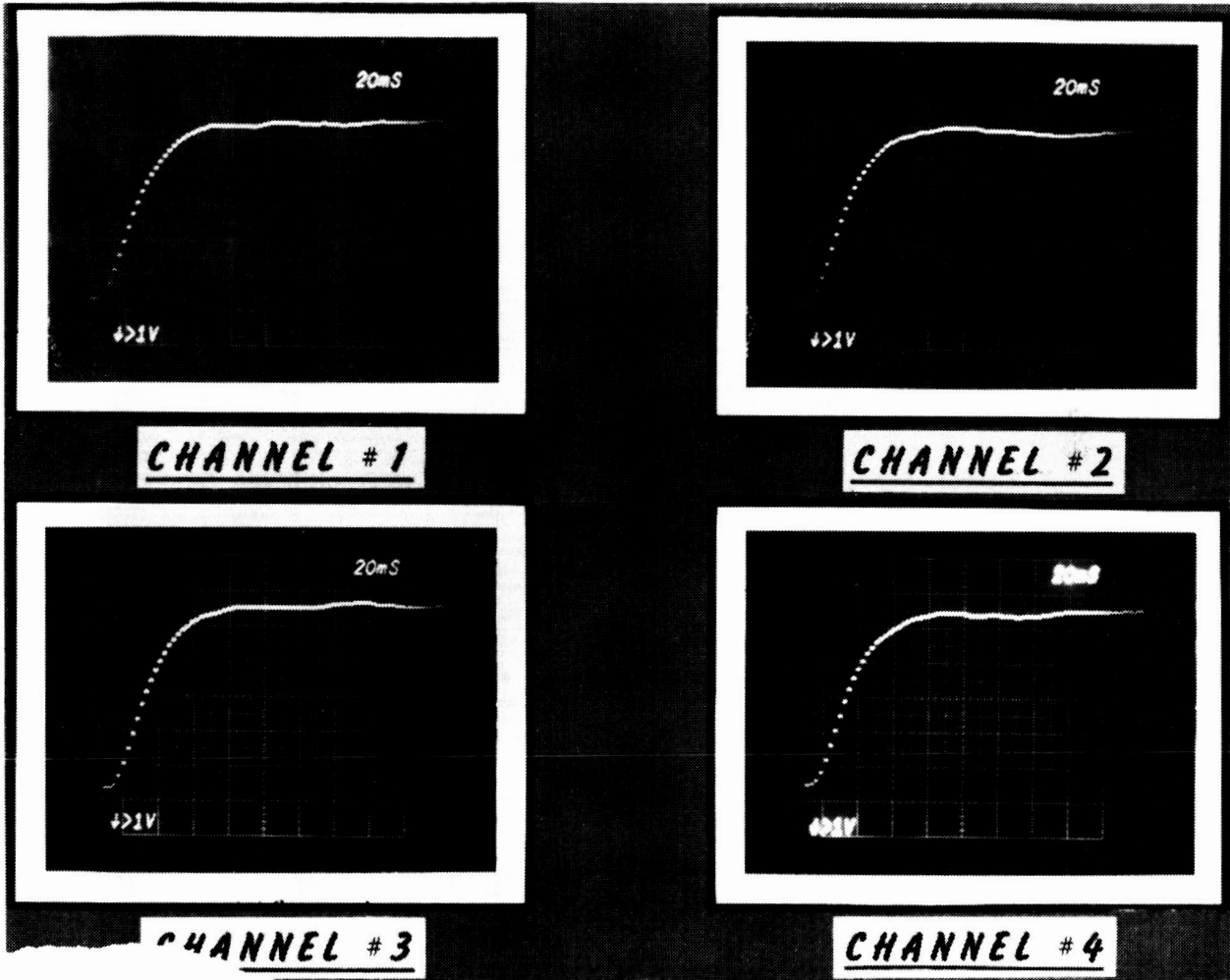
Figure 21.- Radiometer step response.
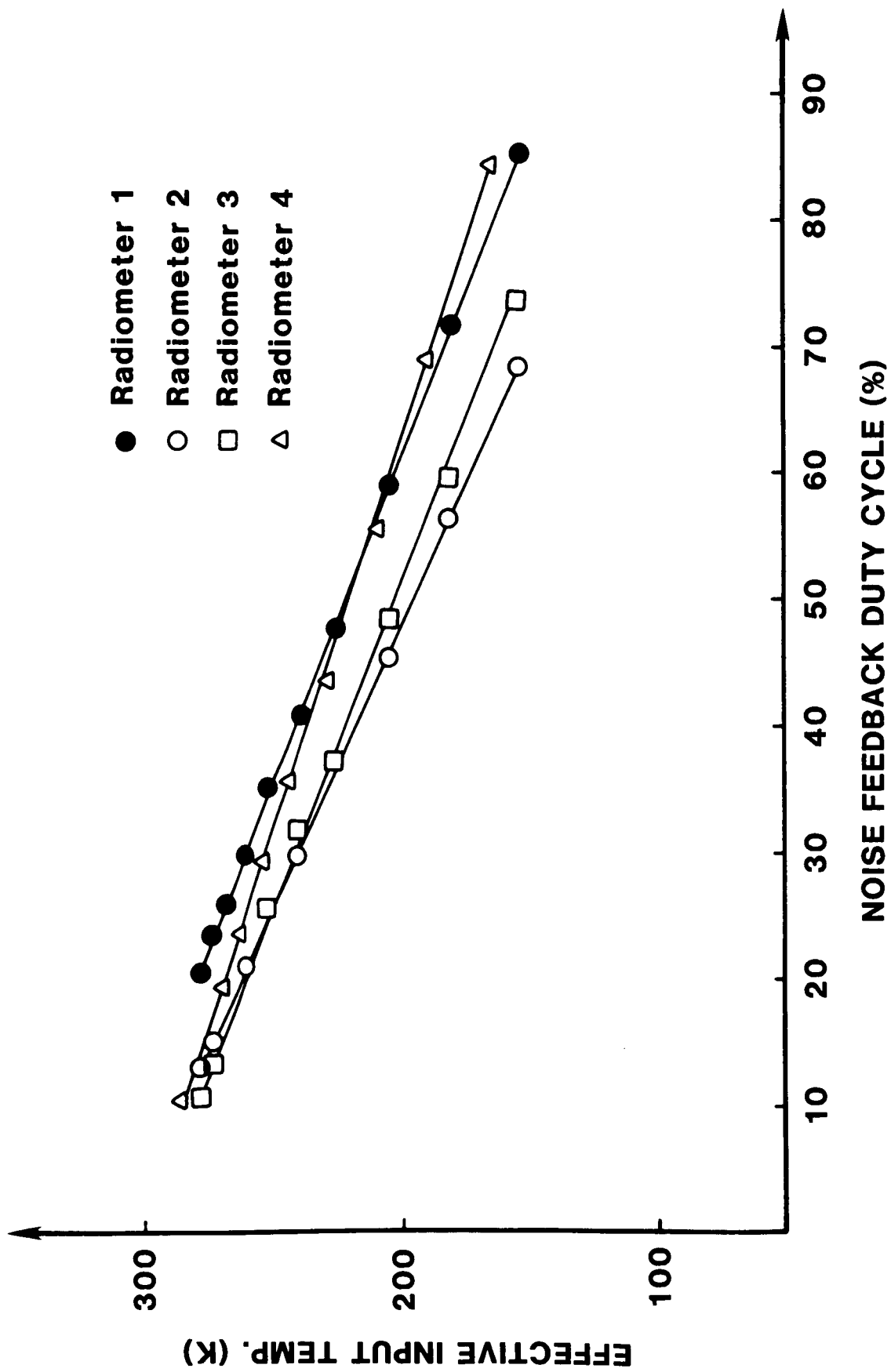
Figure 22.- Laboratory linearity test results.

40
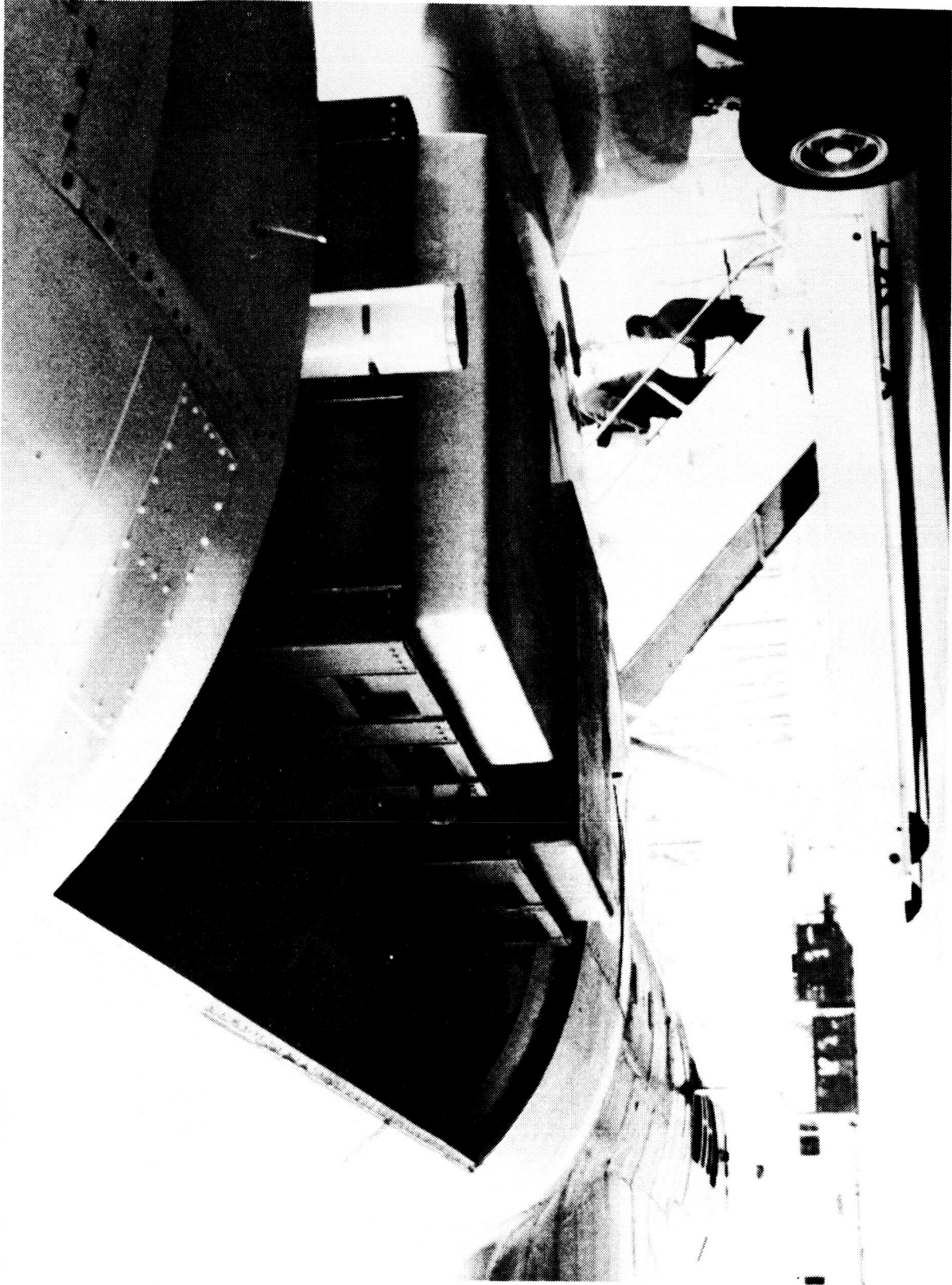
Figure 23.- Flight test aircraft installation.
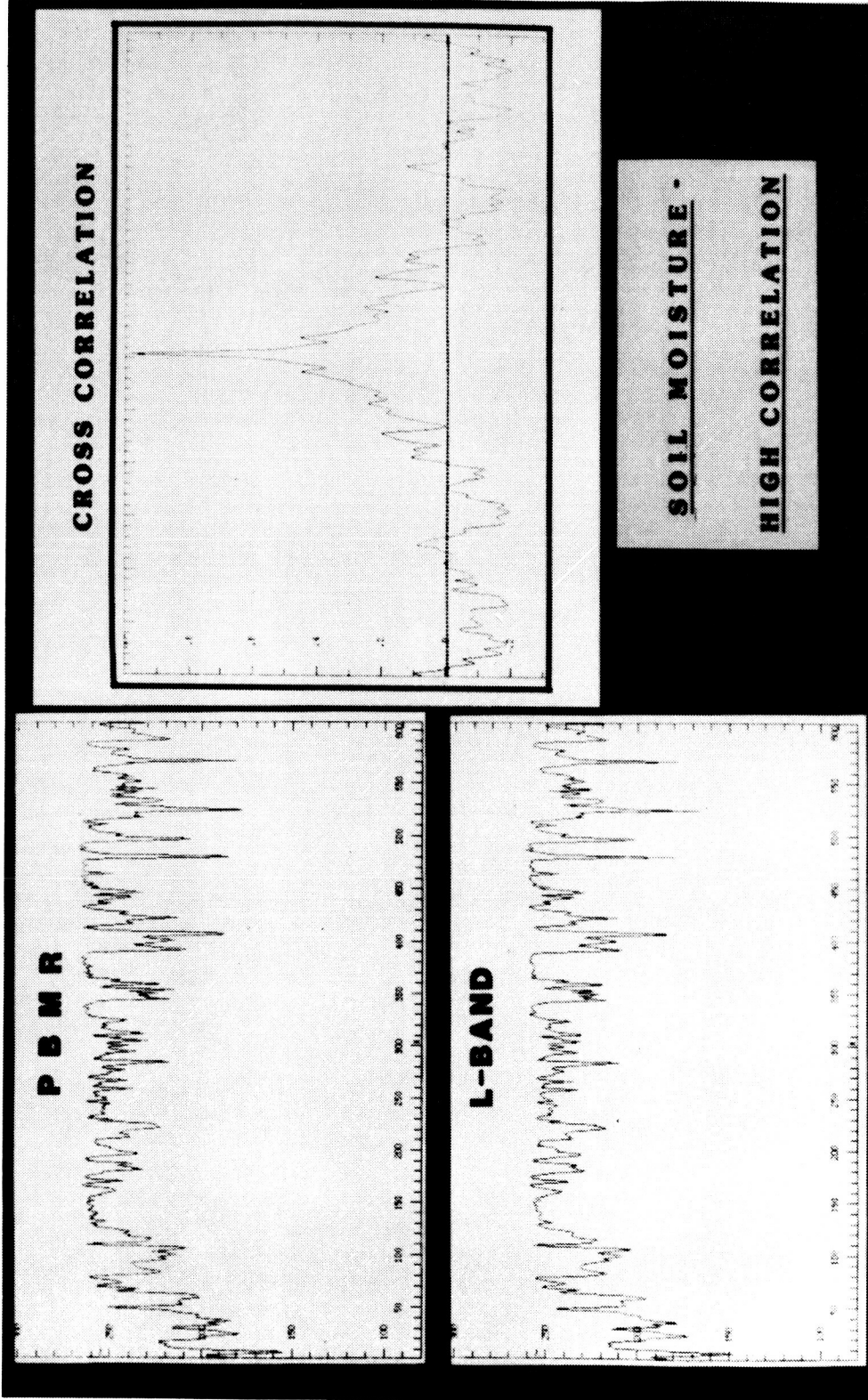
Figure 24.- High contrast flight line.
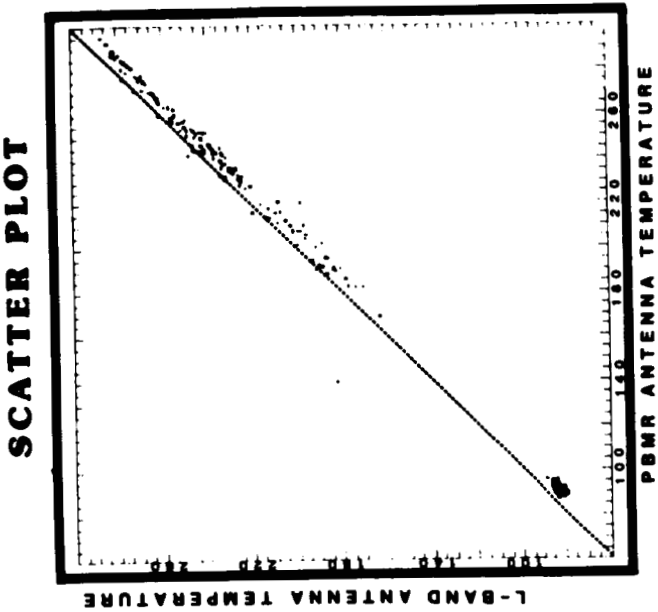
Figure 25.- Land water boundary.
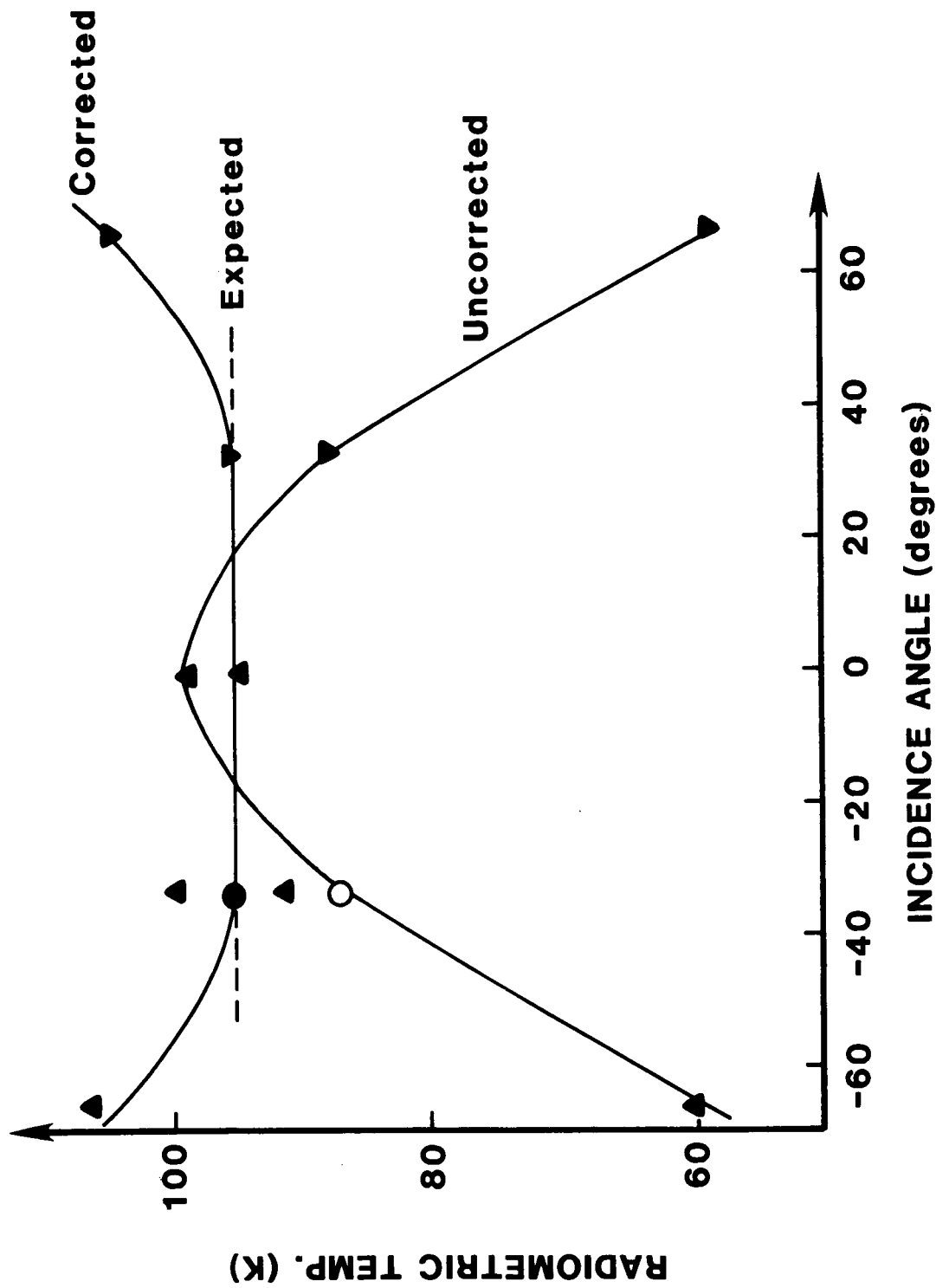
Figure 26.- Antenna pattern correction flight data.
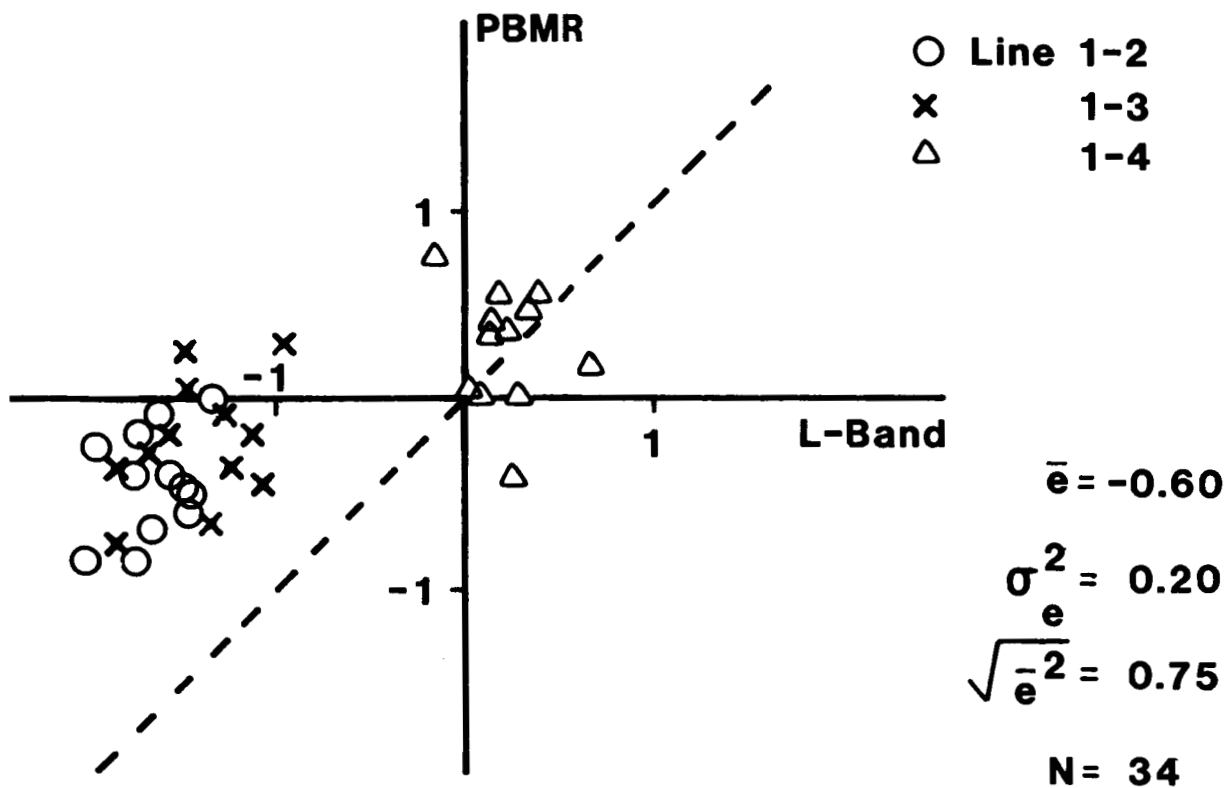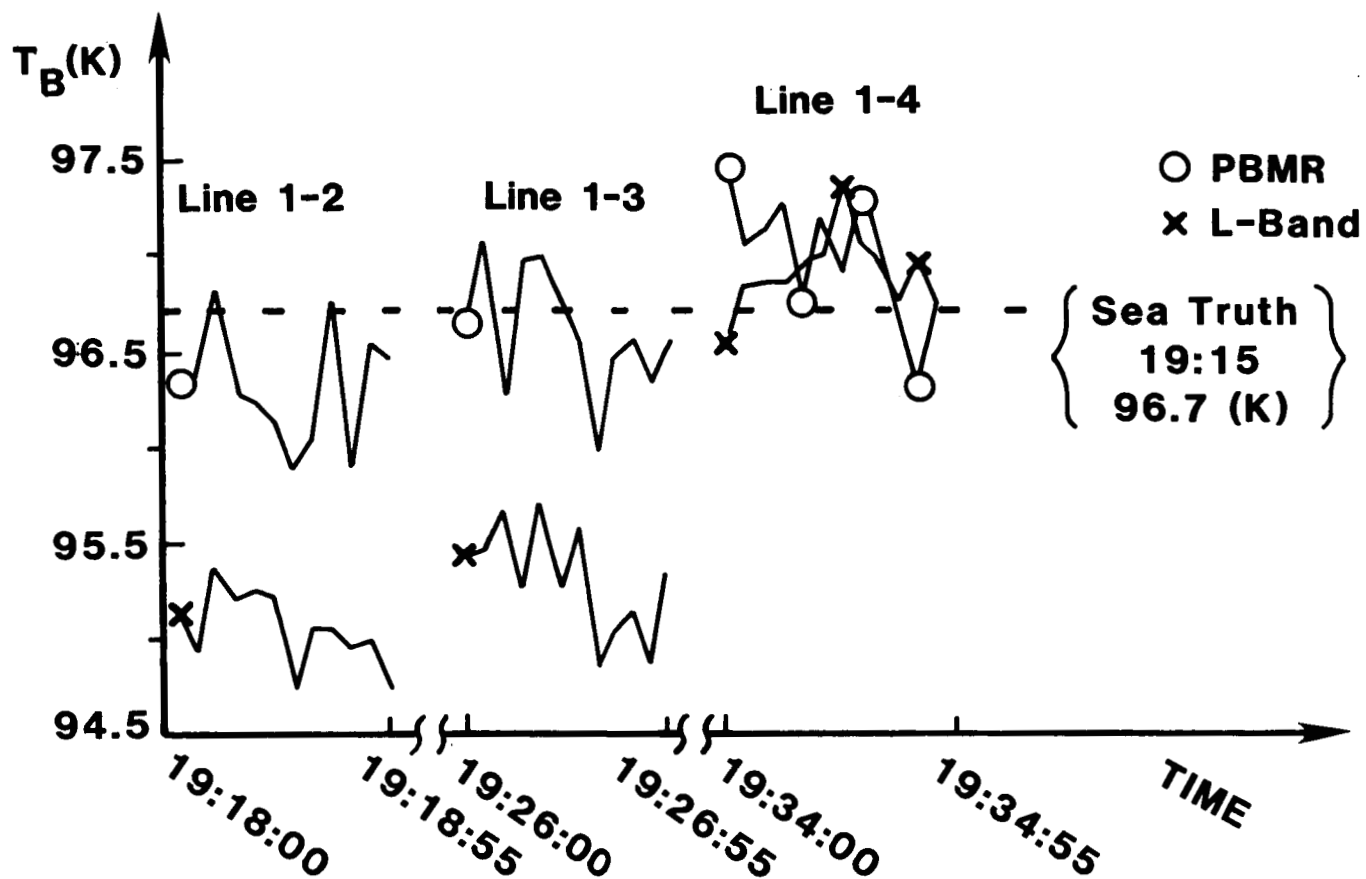
Figure 27.- Sea truth Site 1.
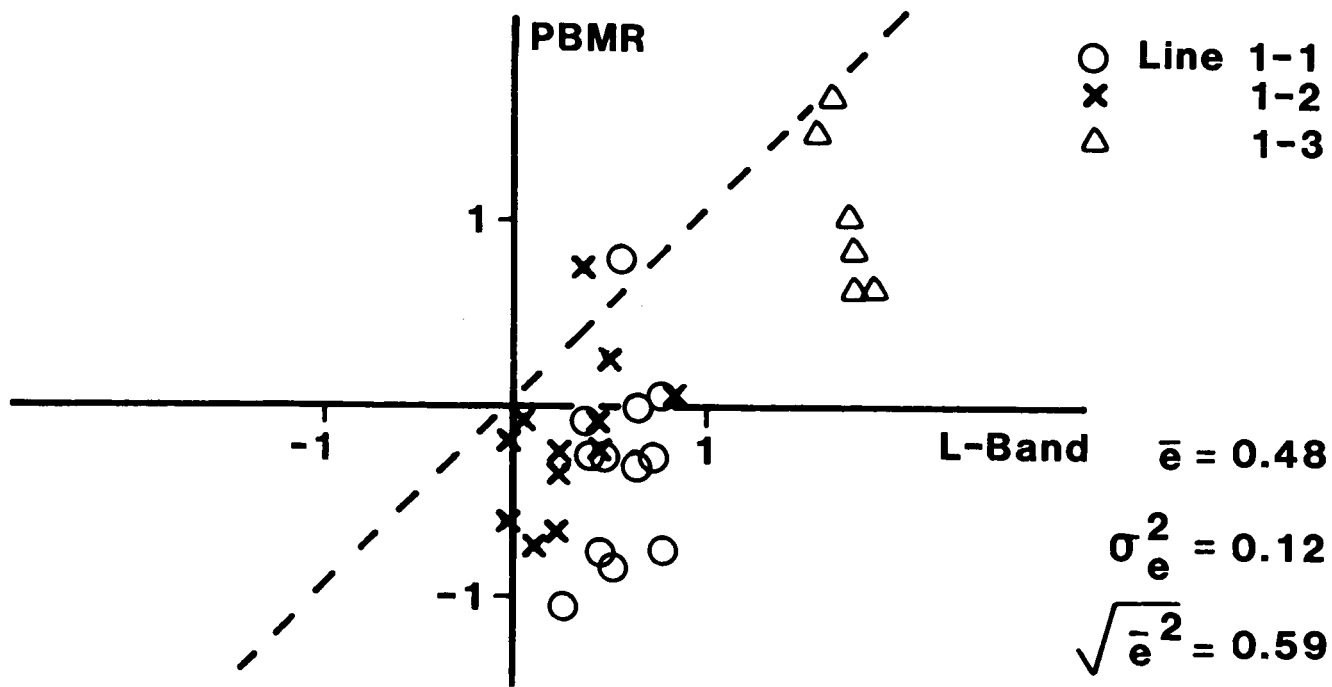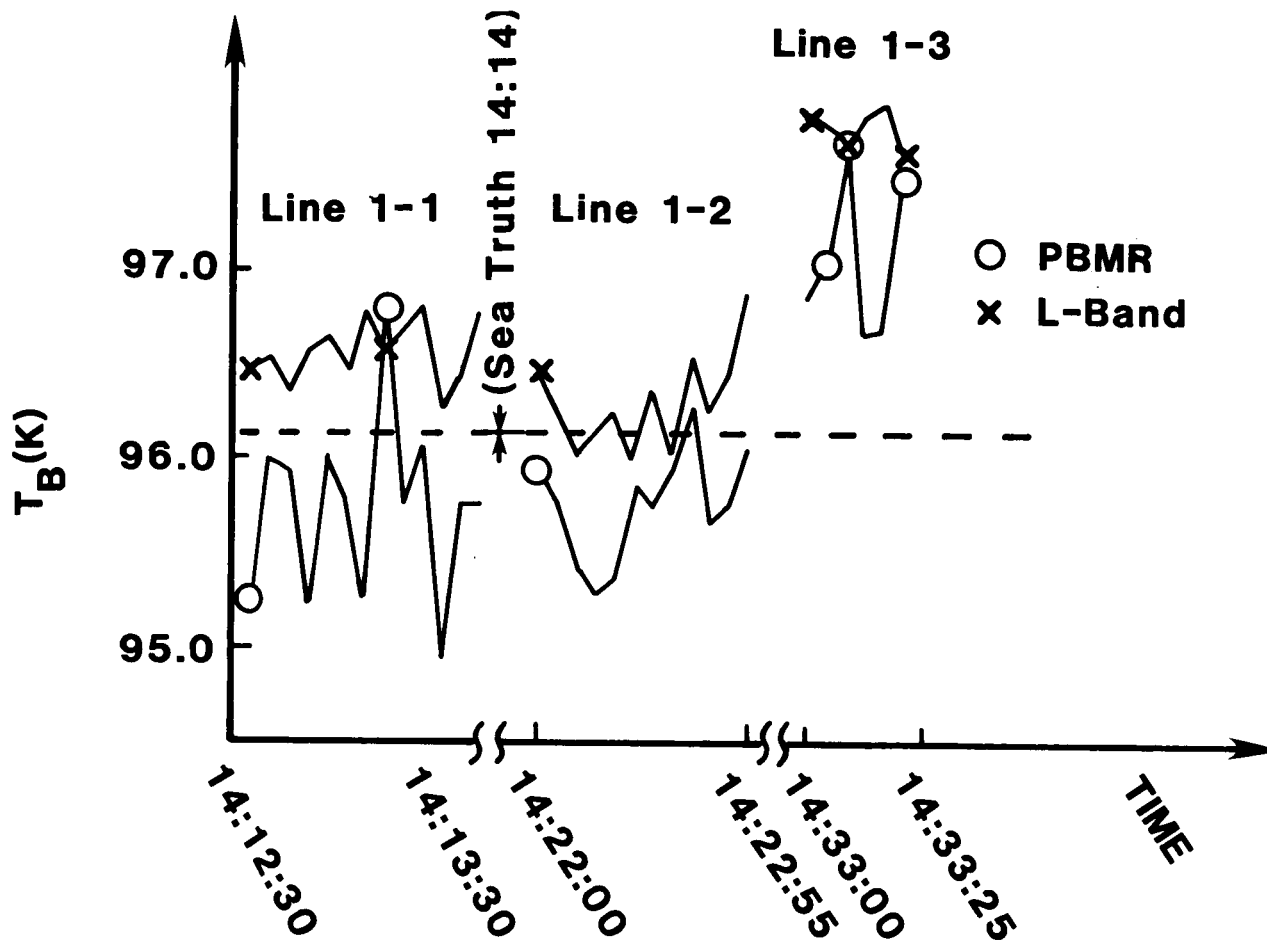
Figure 28.- Sea truth Site 2.
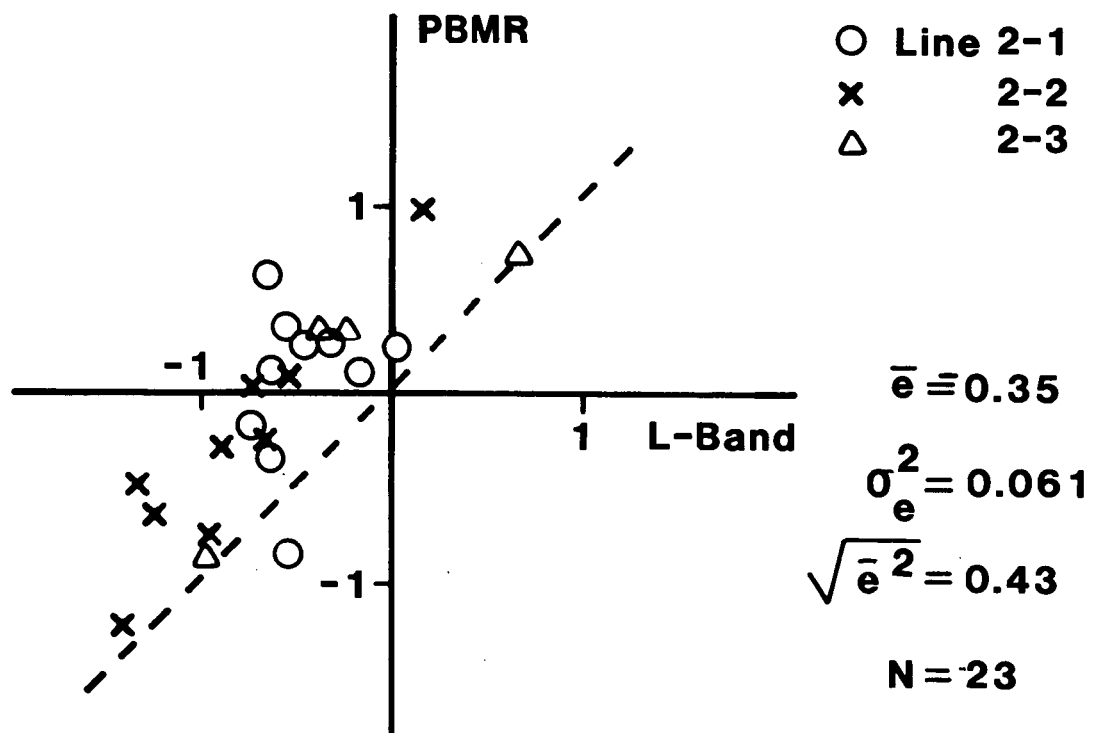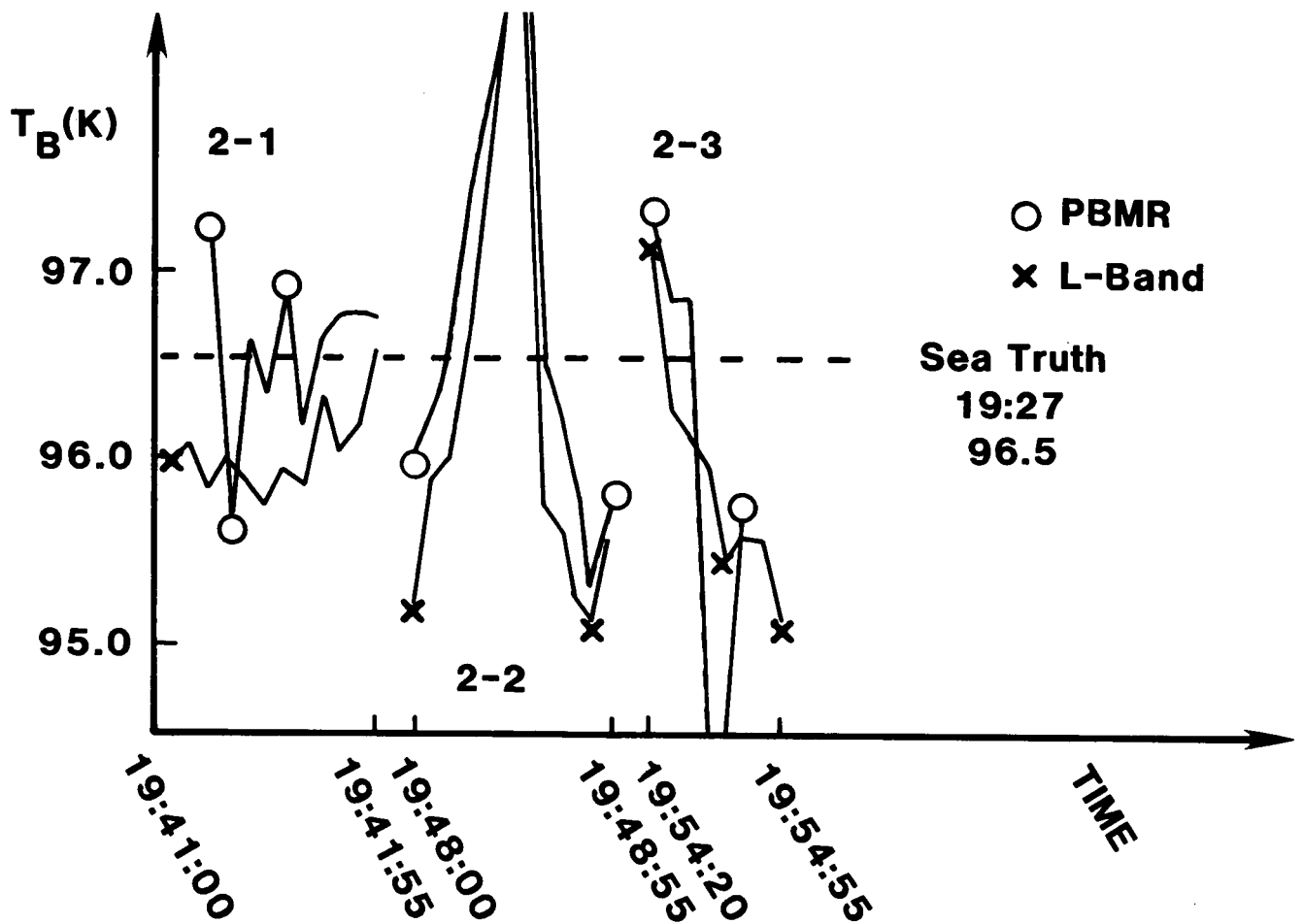
Figure 29.- Sea truth Site 3.
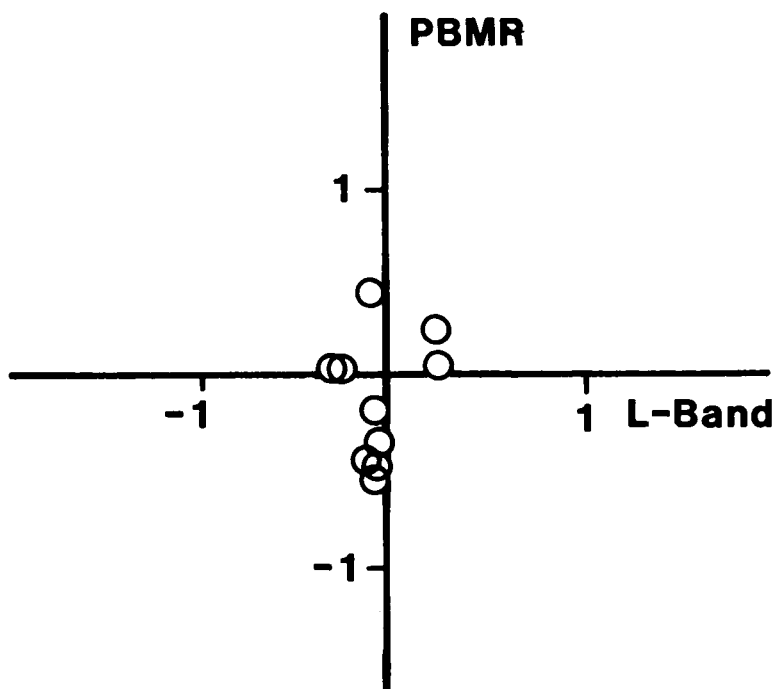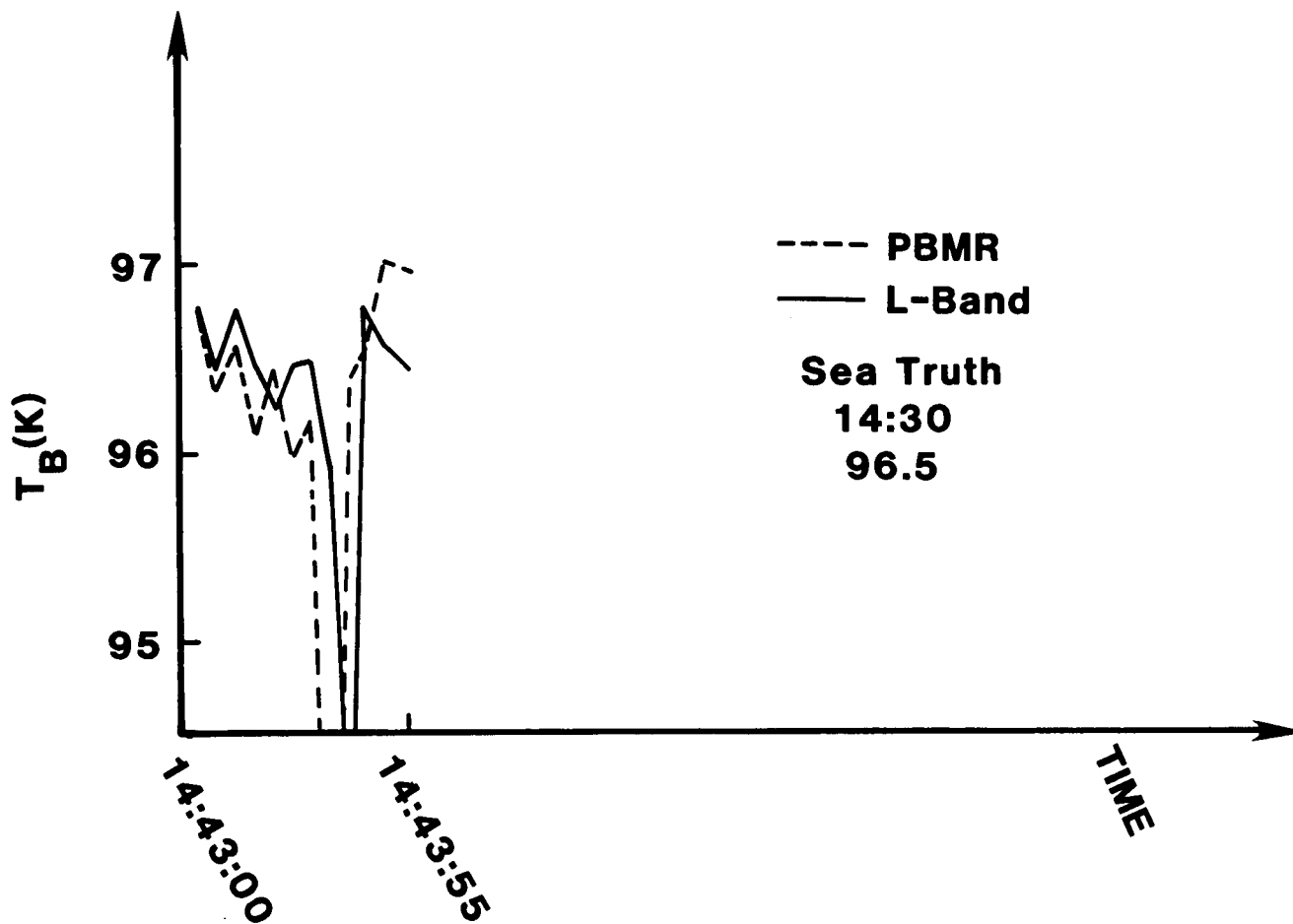
Figure 30.- Sea truth Site 4.
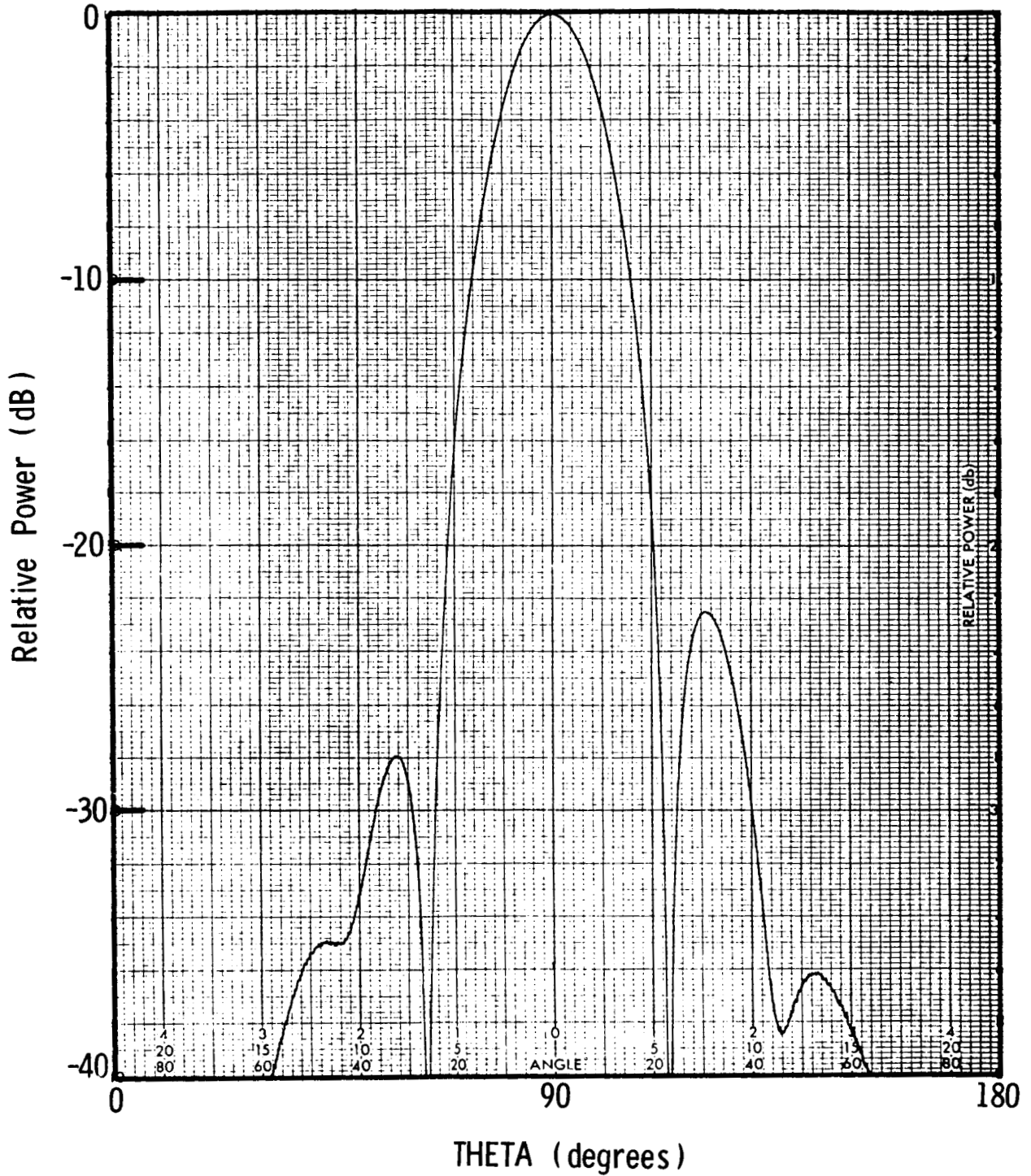
Figure A-1.- Measured P-plane radiation pattern for center beam of 3-beam antenna
array.

49
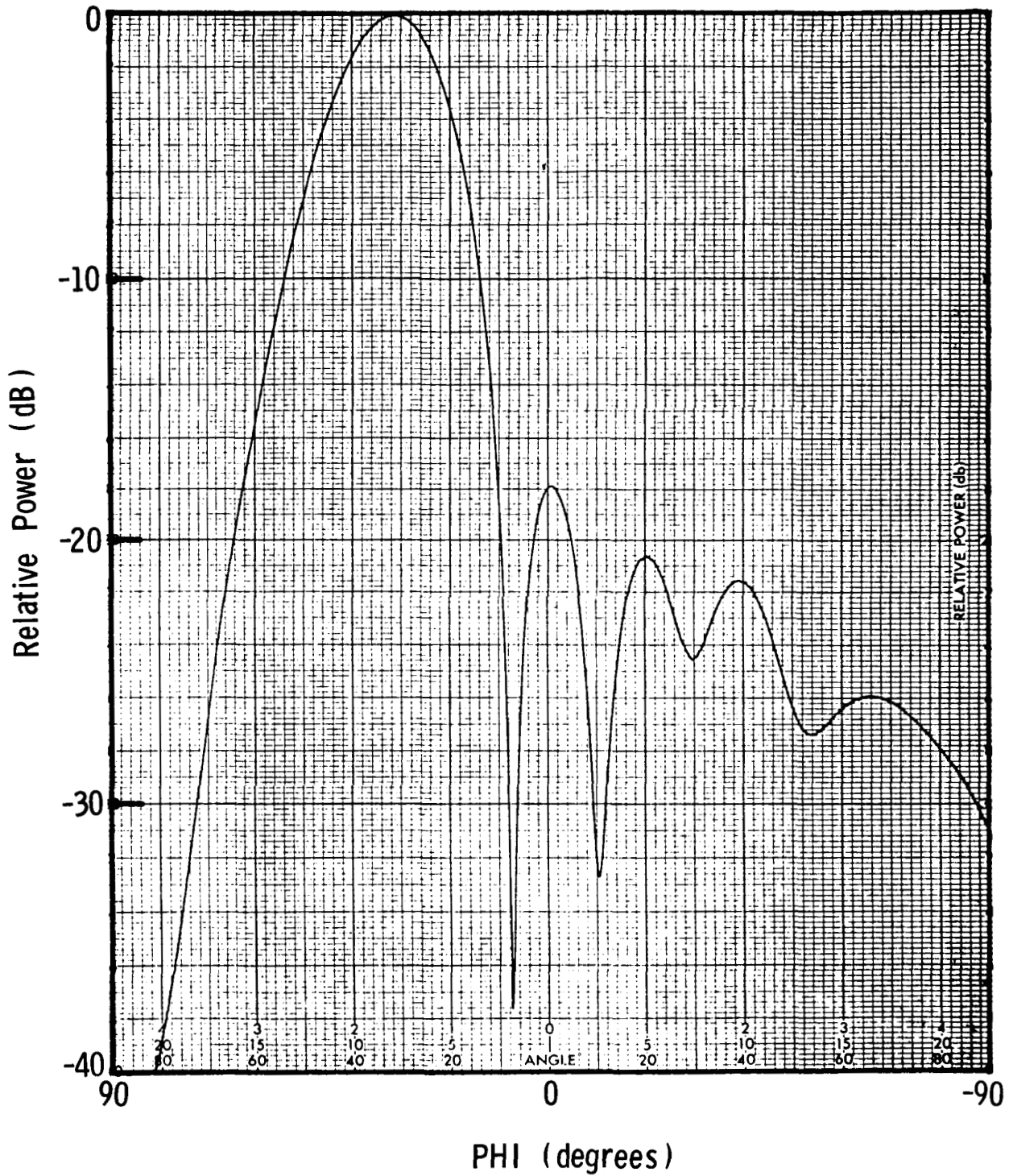
Figure A-2.- Measured H-plane radiation pattern for heap No. 1 of 3-beam antenna array.
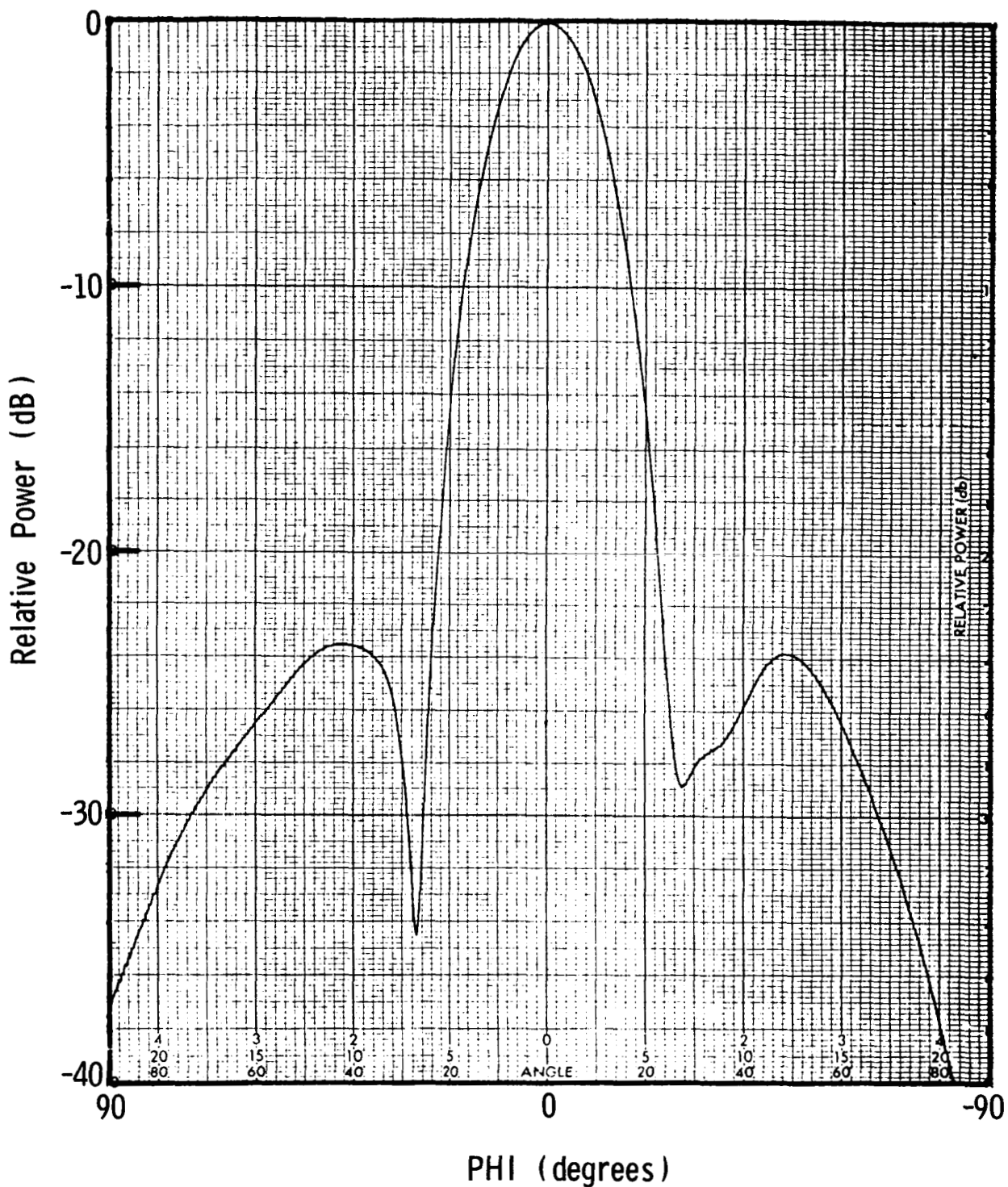
Figure A-3.- Measured H-plane radiation pattern for beam No. 2 of 3-beam antenna array.

51
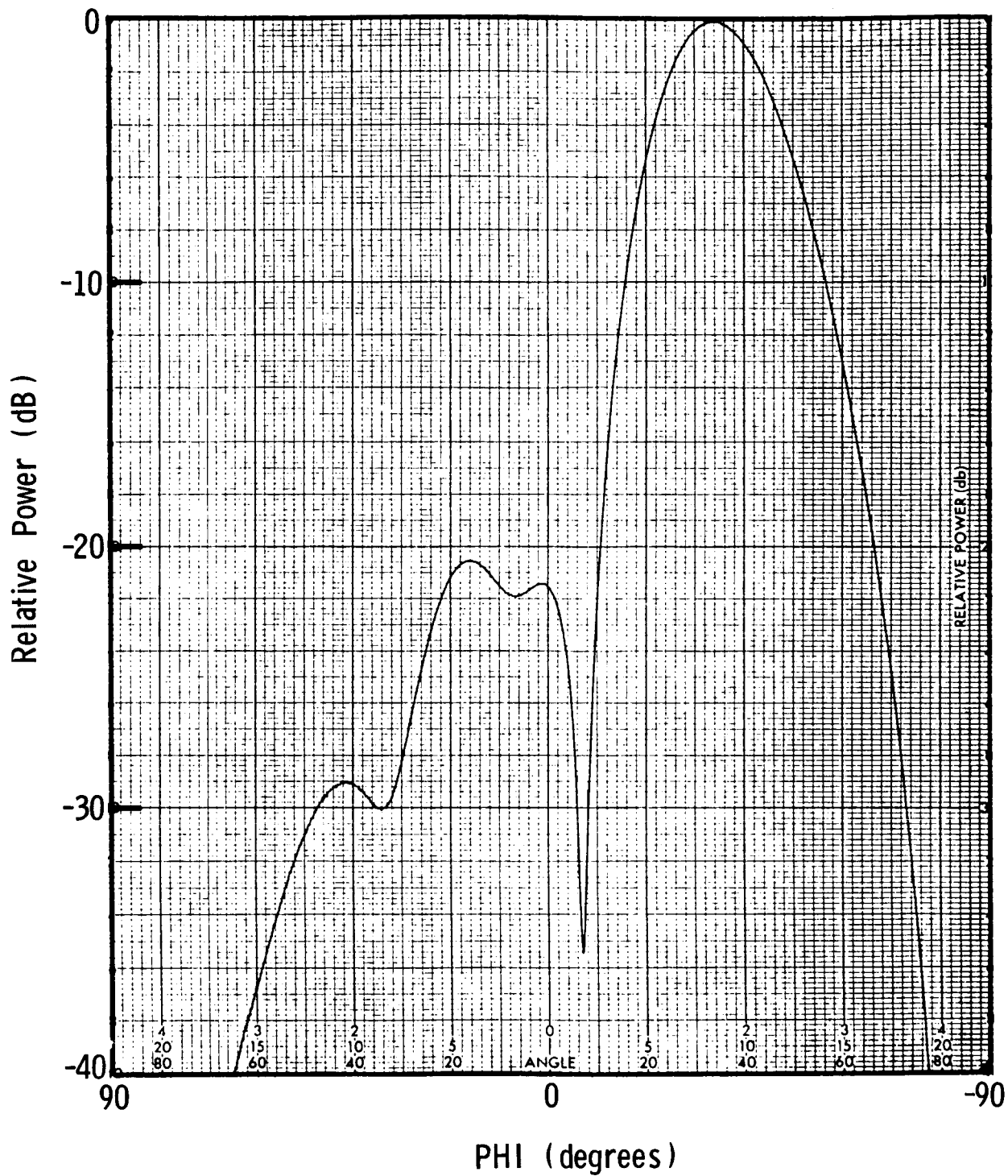
Figure A-4.- Measured H-plane radiation pattern for beam No. 3 of 3-beam antenna
array.
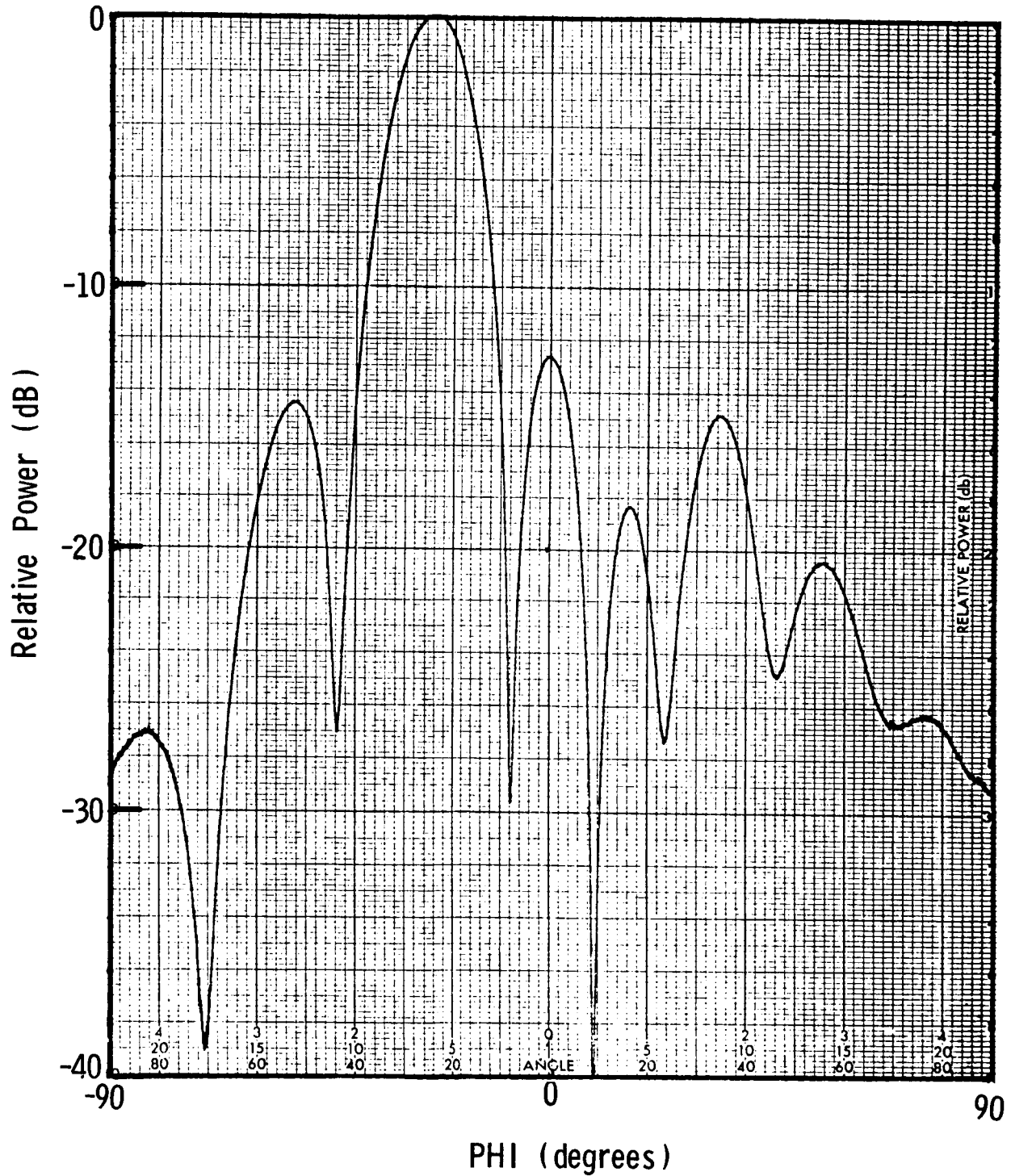
Figure A-5.- Measured H-plane radiation pattern for beam No. 1 of 4-beam antenna
array.
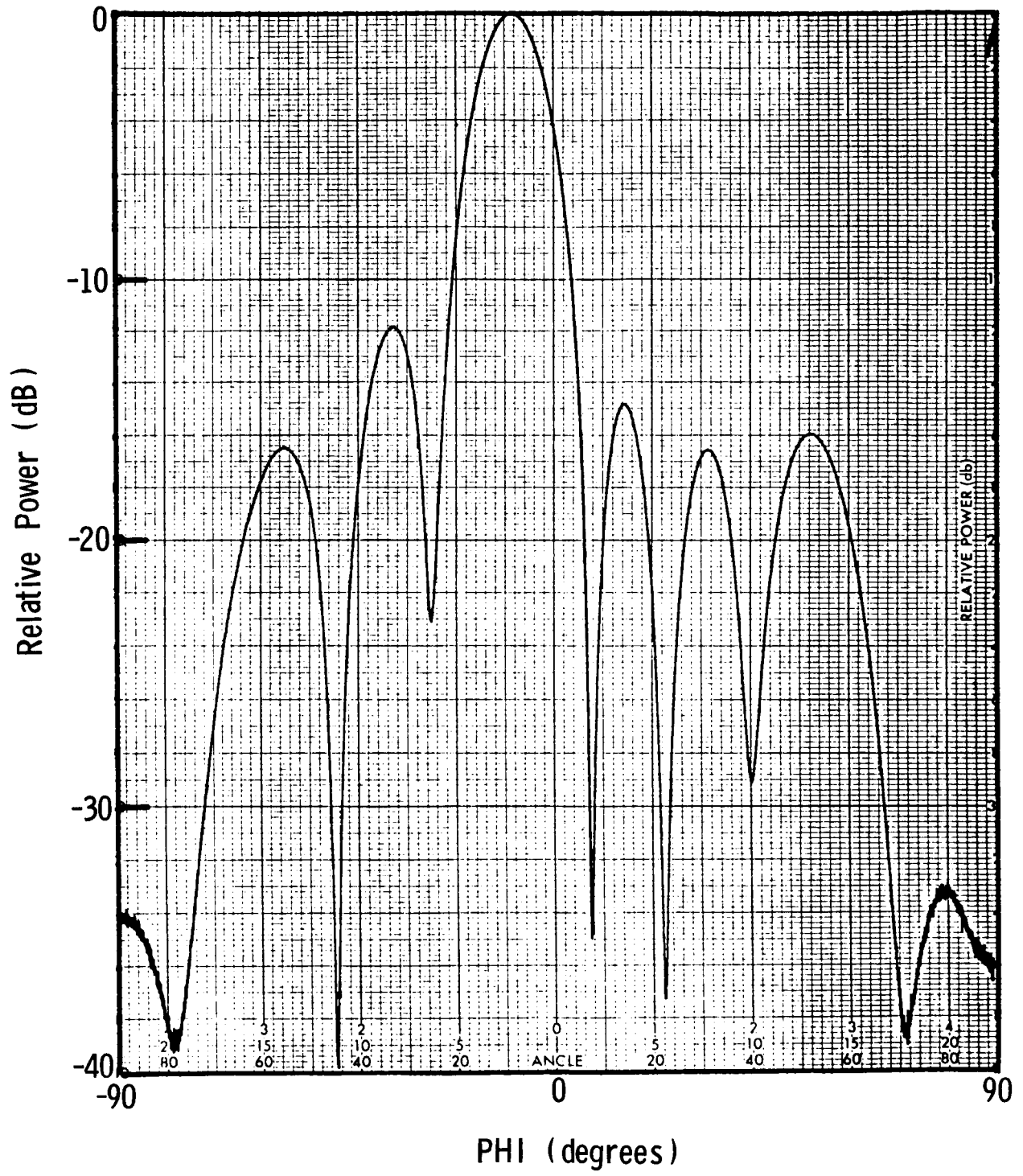
Figure A-6.- Measured H-plane radiation pattern for beam No. 2 of 4-beam antenna array.
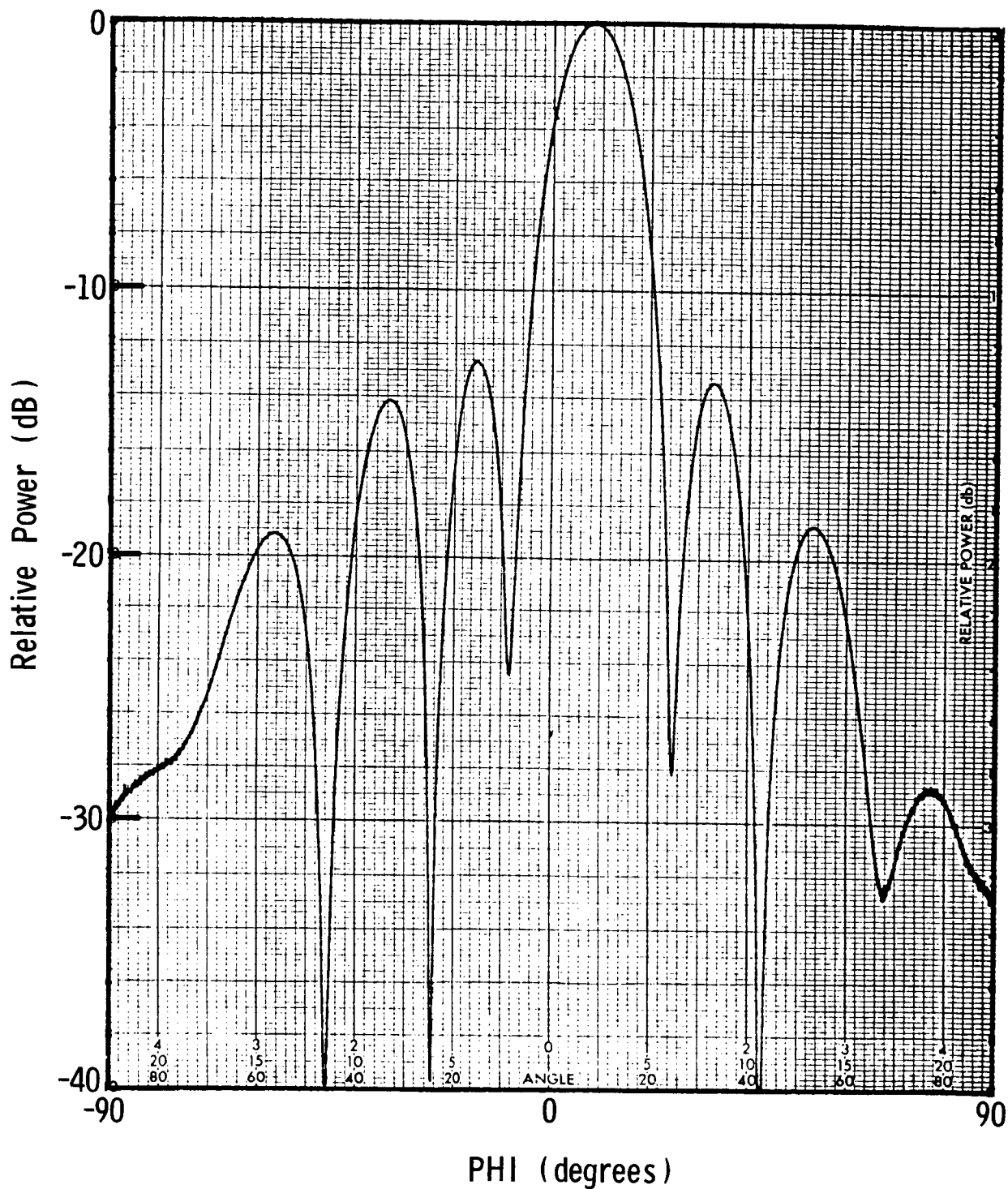
Figure A-7.- Measured H-plane radiation pattern for beam No. 3 of 4-beam antenna array.
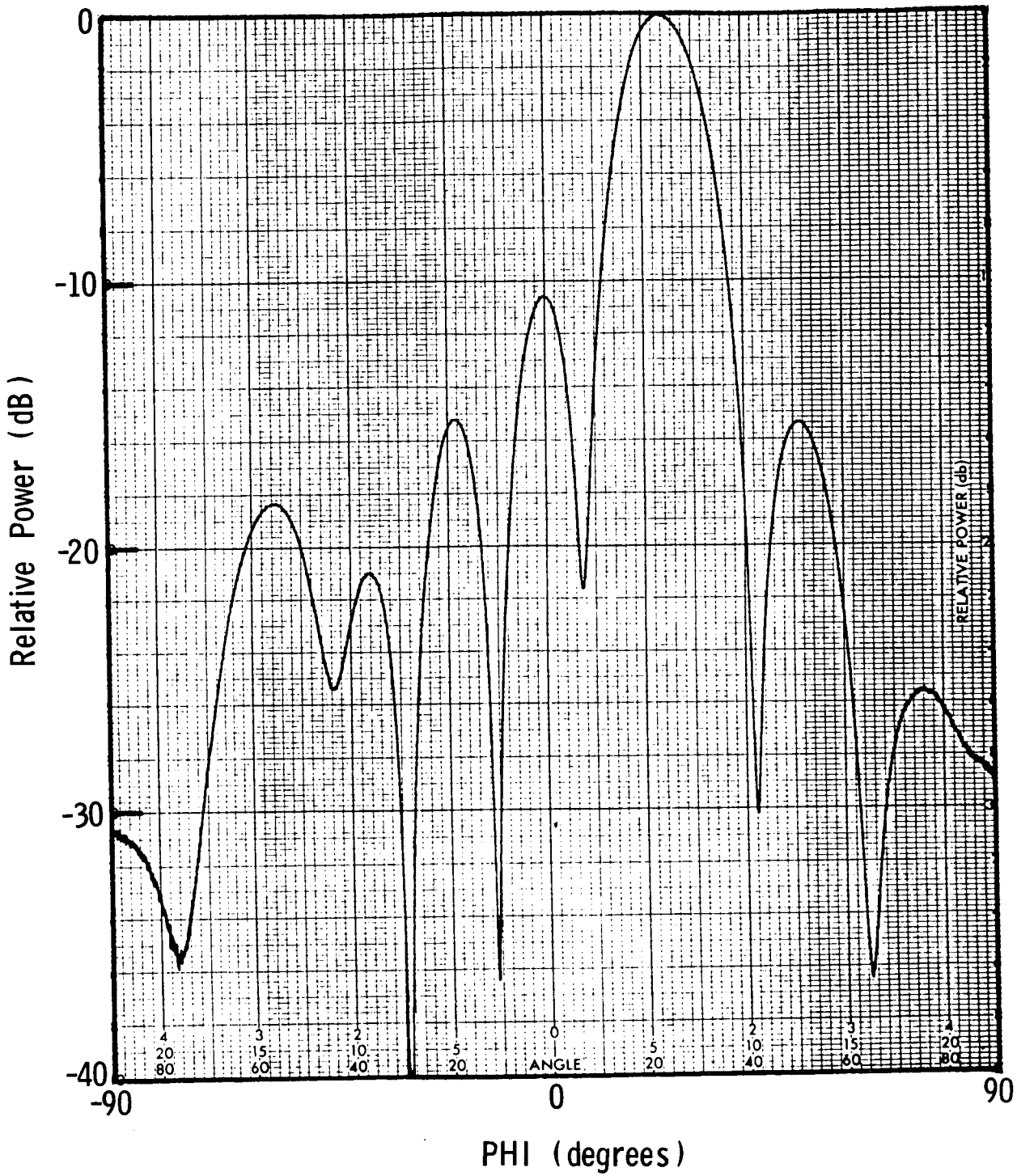
Figure A-8.- Measured H-plane radiation pattern for beam No. 4 of 4-beam antenna array.
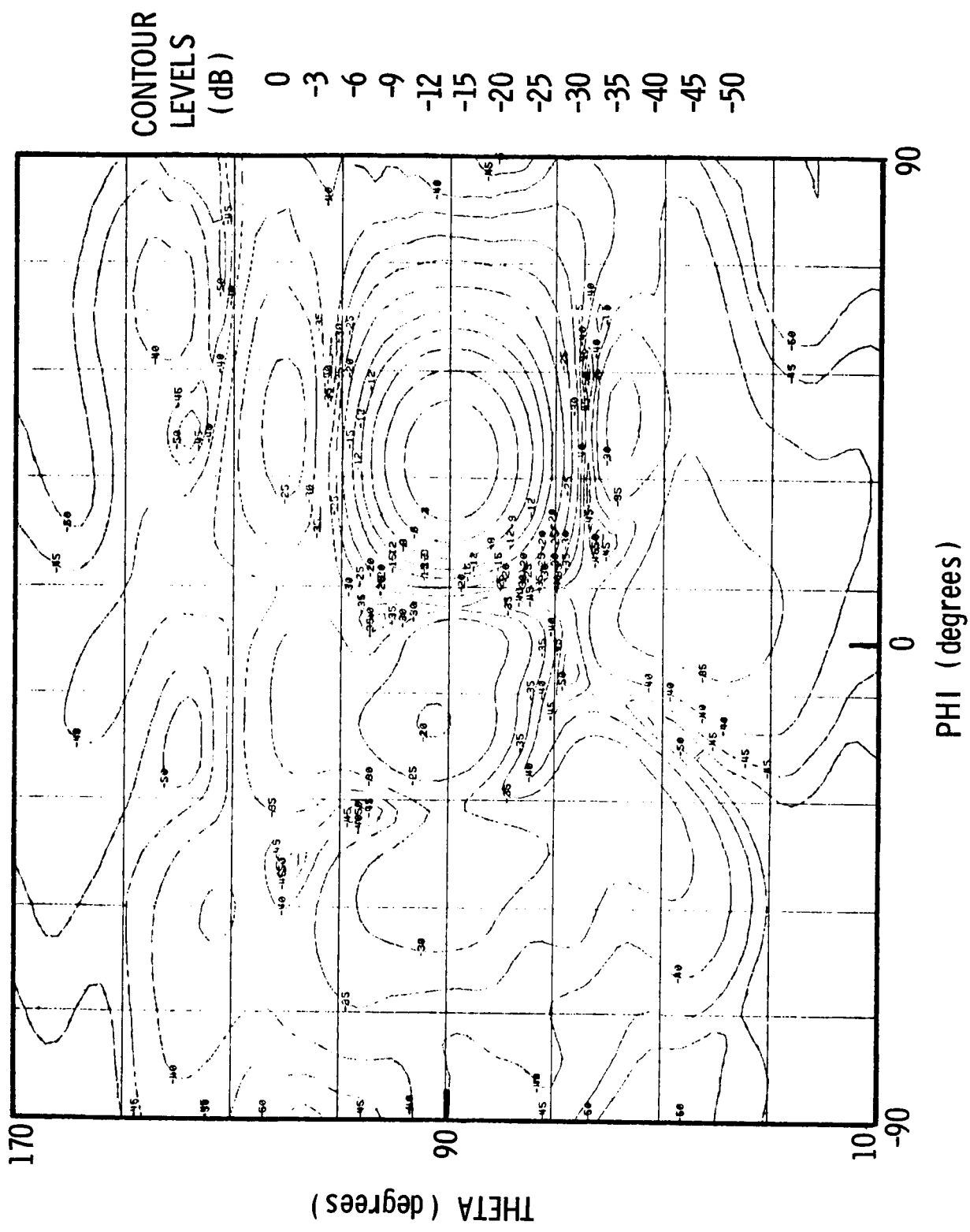
Figure A-9.- Measured contour radiation pattern for beam No. 1 of 3-beam antenna array.

57
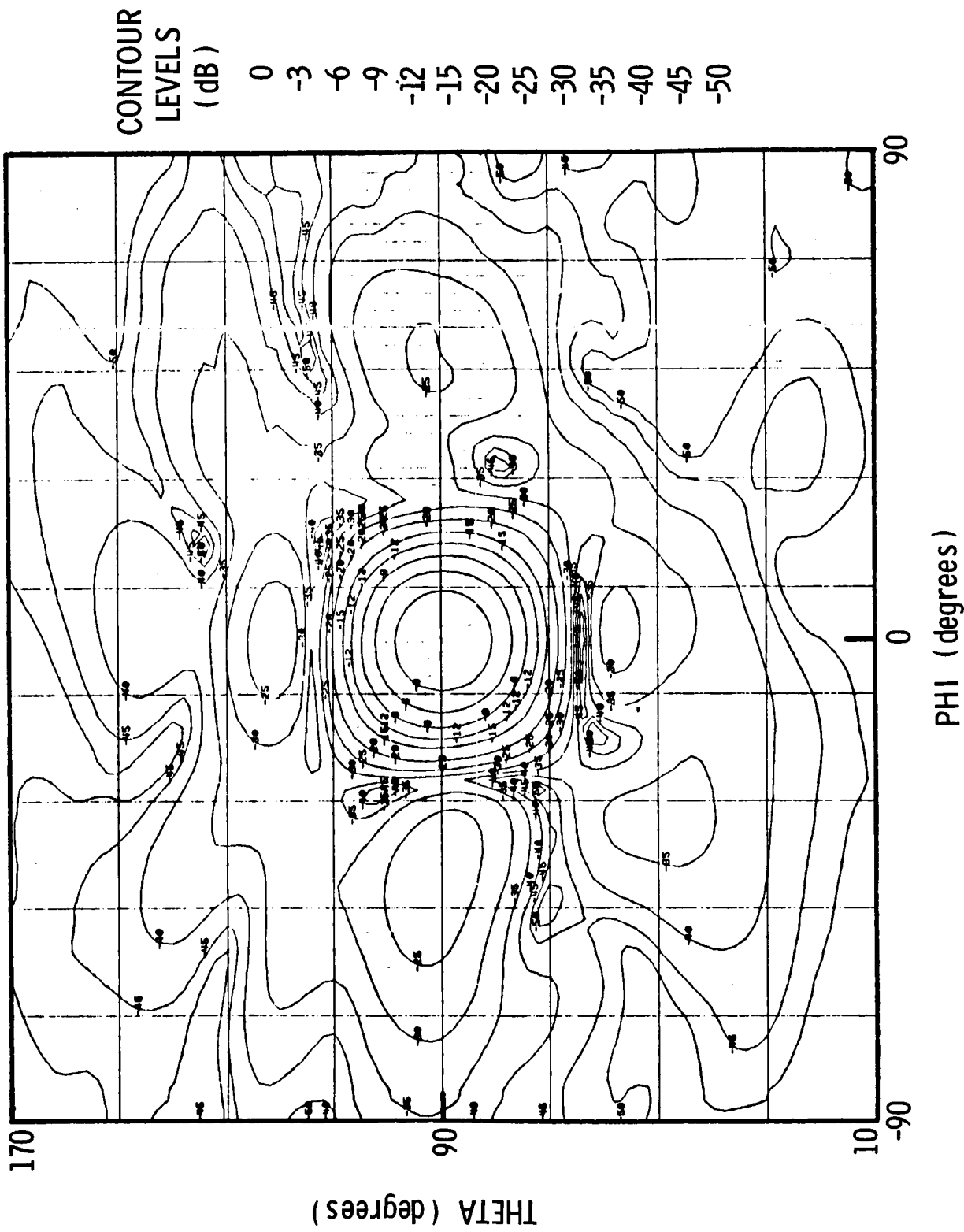
Figure A-10.- Measured contour radiation pattern for beam No. 2 of 3-beam antenna array.
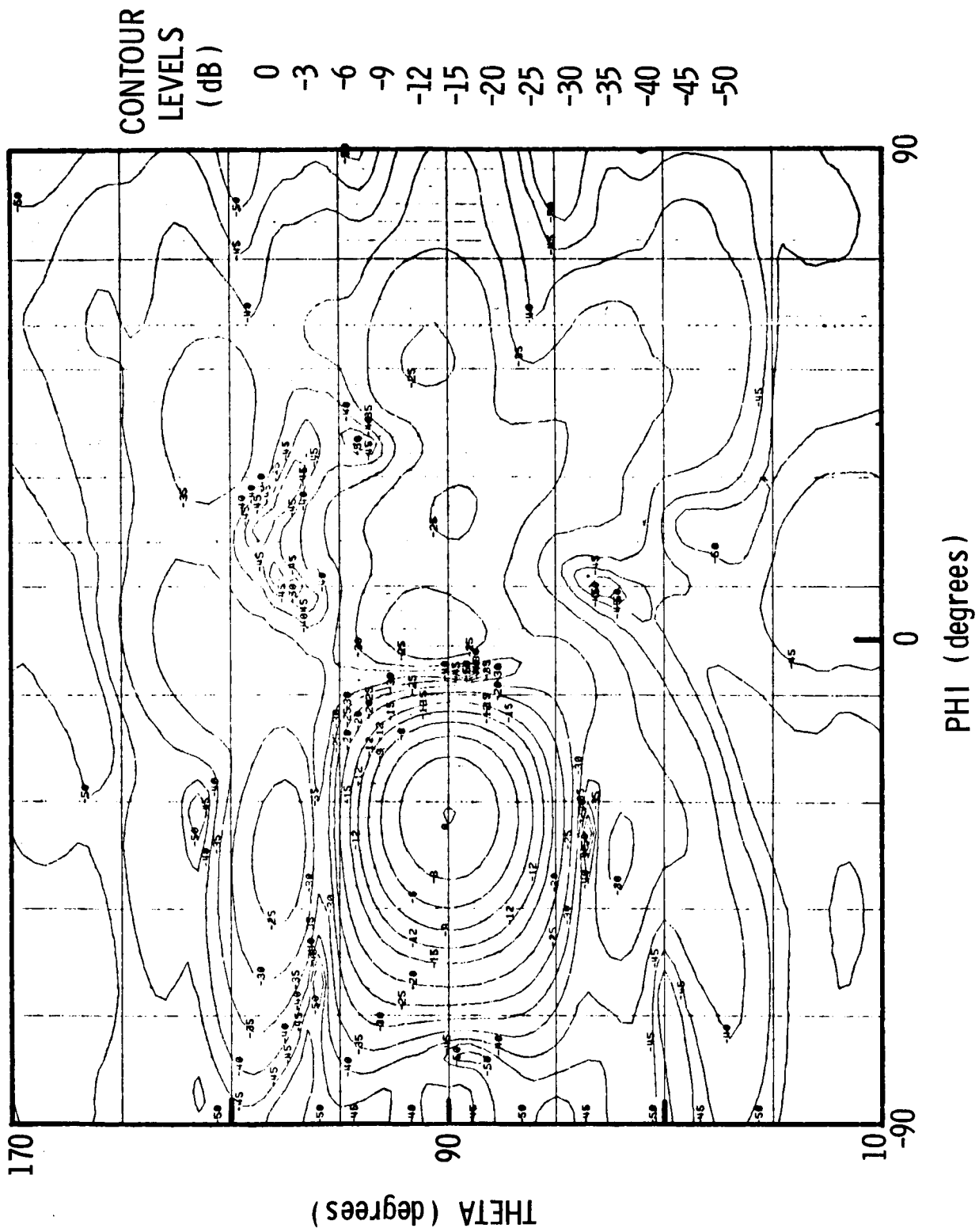
Figure A-11.- Measured contour radiation pattern for beam No. 1 of 3-beam antenna array.
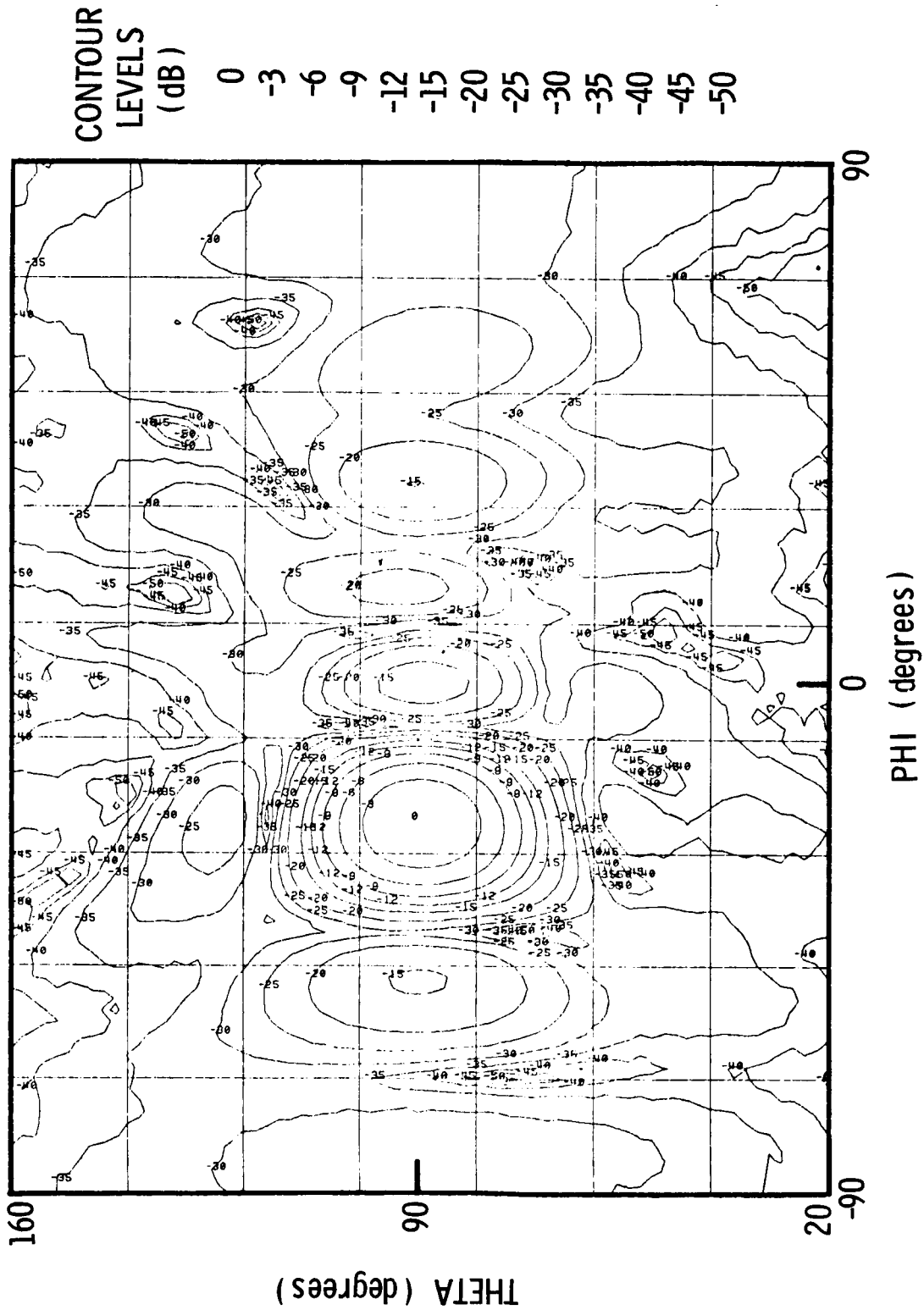
Figure A-12.- Measured contour radiation pattern for beam No. 1 of 4-beam antenna array.
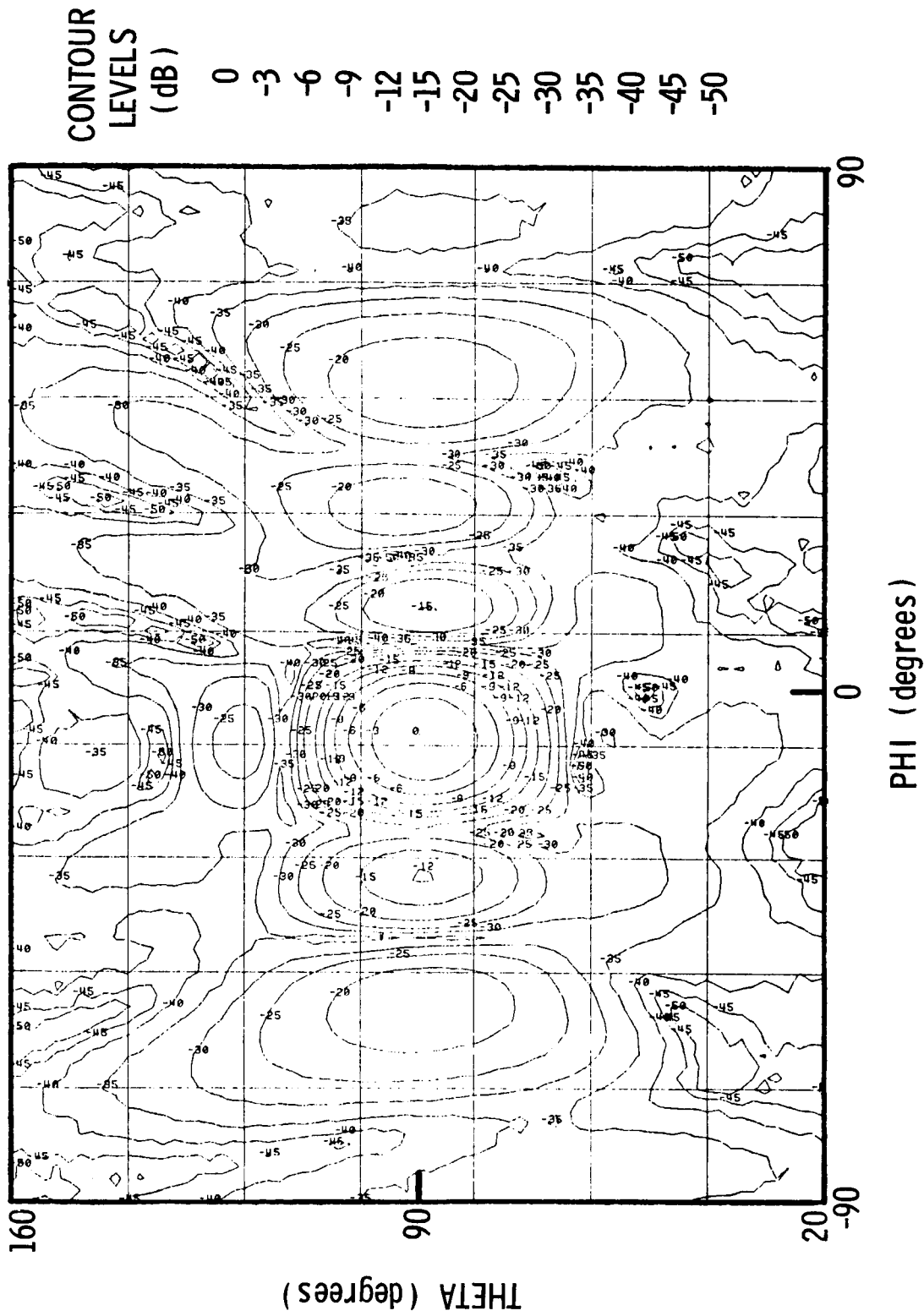
Figure A-13.– Measured contour radiation pattern for beam No. 2 of 4-beam antenna array.

61

CONTOUR
LEVELS
(dB)
0
-3
-6
-9
-12
-15
-20
-25
-30
-35
-40
-45
-50
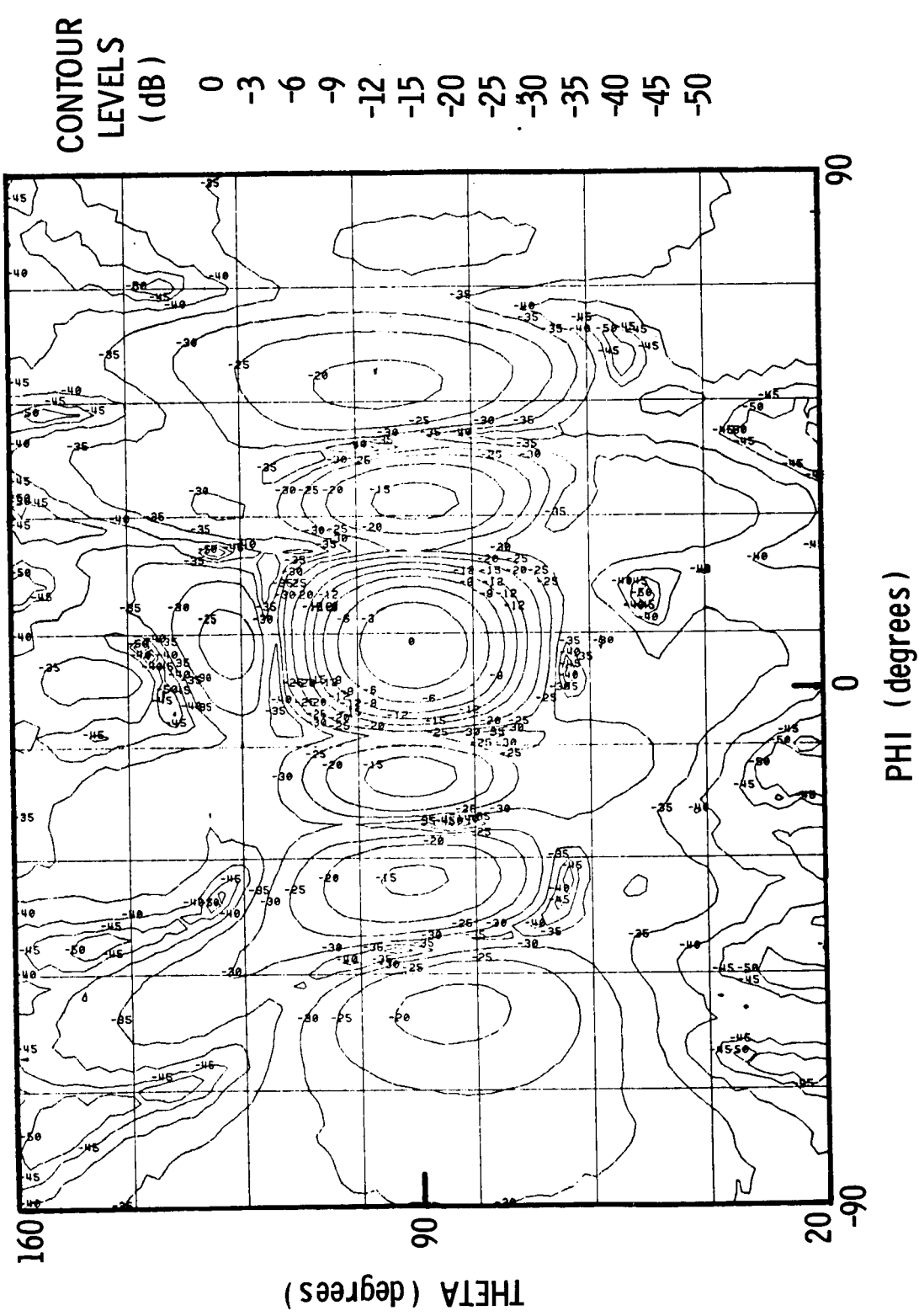
Figure A-14.— Measured contour radiation pattern for beam No. 3 of 4-beam antenna array.
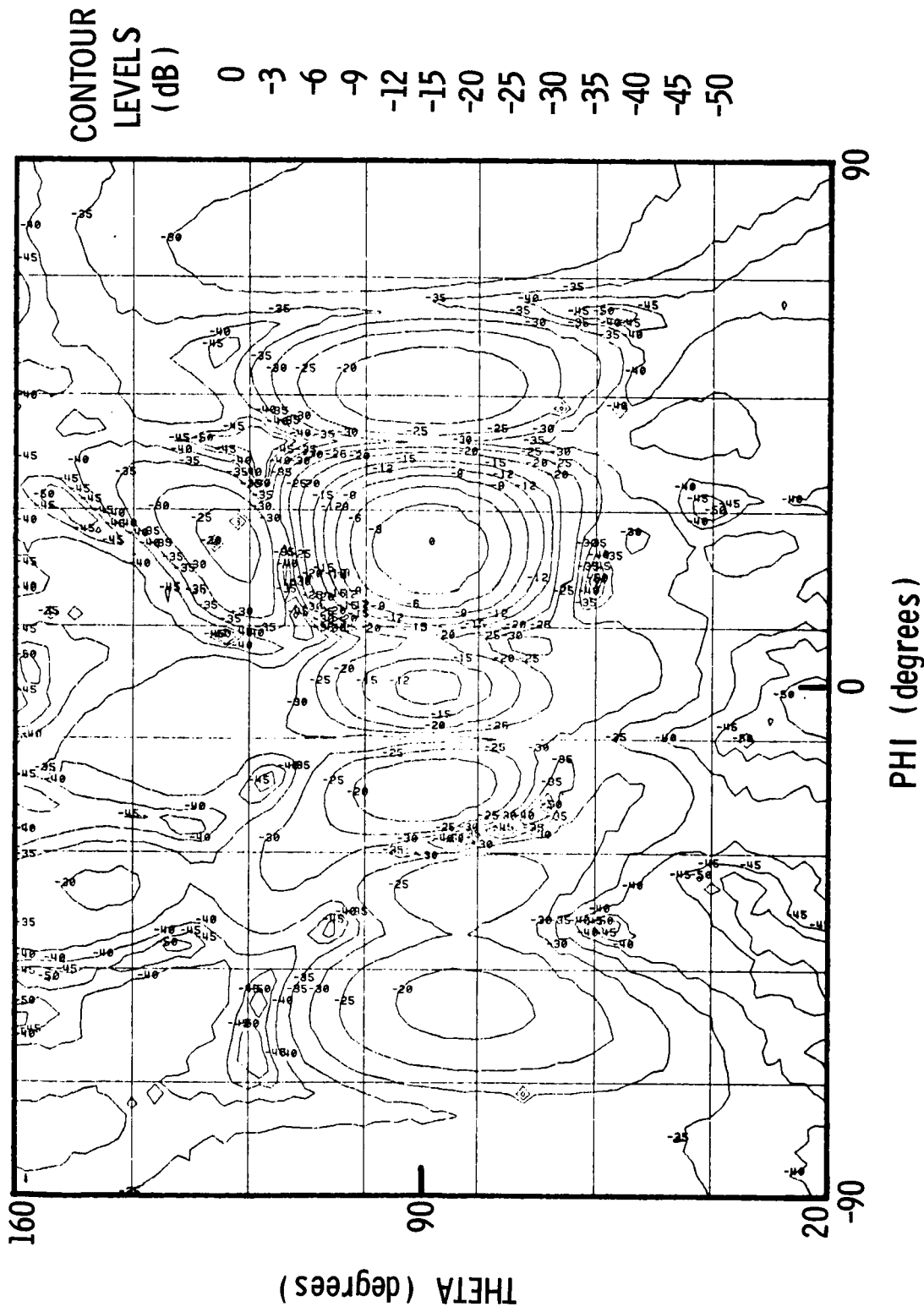
Figure A-15.– Measured contour radiation pattern for beam No. 4 of 4-beam antenna array.

Standard Bibliographic Page

1. Report No. NASA TM-89005	2. Government Accession No.	3. Recipient's Catalog No.
4. Title and Subtitle Design and Development of a Multibeam 1.4 GHz Pushbroom Microwave Radiometer		5. Report Date September 1986
		6. Performing Organization Code 506-44-21-03
7. Author(s) R. W. Lawrence, M. C. Bailey, R. F. Harrington, C. P. Hearn, J. G. Wells and W. D. Stanley		8. Performing Organization Report No.
9. Performing Organization Name and Address NASA Langley Research Center Hampton, Virginia 23665-5225		10. Work Unit No.
		11. Contract or Grant No.
12. Sponsoring Agency Name and Address National Aeronautics and Space Administration Washington, D.C. 20546-0001		13. Type of Report and Period Covered Technical Memorandum
		14. Sponsoring Agency Code

15. Supplementary Notes

R. W. Lawrence, M. C. Bailey, R. F. Harrington, C. P. Hearn, and
   J. G. Wells: Langley Research Center, Hampton, Virginia.
W. D. Stanley: Old Dominion University, Norfolk, Virginia.

16. Abstract

The design and operation of a multiple beam, digital signal processing
radiometer are discussed. The discussion includes a brief description of each
major subsystem and an overall explanation of the hardware requirements and
operation.

A series of flight tests were conducted in which sea-truth sites, as well as,
an existing radiometer were used to verify the Pushbroom Radiometer
performance. The results of these tests indicate that the Pushbroom Radiometer
did meet the sensitivity design goal of 1.0 kelvin, and exceeded the accuracy
requirement of 2.0 kelvin. Additional performance characteristics and test
results are also presented.

17. Key Words (Suggested by Authors(s)) Radiometer Pushbroom Radiometer Digital Radiometer Imaging Radiometer	18. Distribution Statement Unclassified - Unlimited Subject Category 33		
19. Security Classif.(of this report) Unclassified	20. Security Classif.(of this page) Unclassified	21. No. of Pages 64	22. Price A04

For sale by the National Technical Information Service, Springfield, Virginia 22161

NASA Langley Form 63 (June 1985)